


Topological states of multiband superconductors with interband pairing

Maximilian F. Holst¹, Manfred Sigrist¹ and Kirill V. Samokhin^{2,*}

¹*Institute for Theoretical Physics, ETH Zurich, 8093 Zurich, Switzerland*

²*Department of Physics, Brock University, Saint Catharines, Ontario, Canada L2S 3A1*

 (Received 20 October 2023; revised 13 February 2024; accepted 27 March 2024; published 30 April 2024)

We study the effects of interband pairing in two-band s -wave and d -wave superconductors with D_{4h} symmetry in both time-reversal invariant as well as time-reversal symmetry-breaking states. The presence of interband pairing qualitatively changes the nodal structure of the superconductor: nodes can (dis)appear, merge, and leave high-symmetry locations when interband pairing is tuned. Furthermore, in the d -wave case, we find that also the boundary modes change qualitatively when interband pairing increases: flat zero-energy Andreev bound states gap out and transition to helical edge states.

DOI: [10.1103/PhysRevResearch.6.023105](https://doi.org/10.1103/PhysRevResearch.6.023105)

I. INTRODUCTION

The properties of multiband, in particular two-band, superconductors (SCs) have recently emerged as a subject of substantial interest in condensed matter physics. Starting with the discovery of superconductivity in MgB_2 [1,2], the list of SCs in which multiband or multiorbital effects play an important role has been steadily growing and now includes numerous materials, such as nickel borocarbides [3], Sr_2RuO_4 [4–6], $NbSe_2$ [7] and other transition metal dichalcogenides [8], the heavy-fermion compounds $CeCoIn_5$ [9] and $CePt_3Si$ [10], iron-based SCs [11,12], doped topological insulators [13,14], and others.

Theoretically, a two-band generalization of the Bardeen-Cooper-Schrieffer (BCS) model was introduced in Refs. [15,16]. Under the assumption that the Cooper pairs are formed by the quasiparticles in the same band, i.e., intraband Cooper pairs, the order parameter in a one-dimensional (1D) pairing channel, such as s -wave or d -wave, has two components, η_1 and η_2 , which describe the pairing state in each of the two bands. The interband scattering of the Cooper pairs between the bands couples the two order parameters as $\eta_1^* \eta_2 + c.c.$ in the lowest order within a Ginzburg-Landau (GL) expansion, analogous to the Josephson tunneling. Depending on the sign of the scattering matrix element (the coefficient of the GL coupling term), the relative phase between η_1 and η_2 in the uniform ground state is either 0 or π , corresponding to a time-reversal (TR) invariant combination. Subsequent studies have shown that the most significant qualitative differences from the single-band case are connected with the spatial and temporal variations of

the relative phase, which produce such novel features as the Leggett modes [17], phase solitons [18], and fractional vortices [19] (see for a review Ref. [20]).

Recent experimental and theoretical developments have motivated a further extension of the standard theory of multiband superconductivity, by taking into account the pairing among quasiparticles from different bands, i.e., the interband pairing. Within the BCS approach of pairing in the momentum space, interband pairing is feasible if the pairing interaction cutoff energy exceeds the band splitting. Alternatively, starting from a real-space pairing interaction involving different atomic orbitals in a crystalline lattice, we find interband pairing components after transformation into the band representation [21–27], or the interband pairs arise by the proximity effect [28]. Assuming that interband pairs are stabilized through a suitable microscopic mechanism, one can characterize their condensate by an additional order parameter component. Thus, a complete phenomenological description of a two-band SC involves a GL free energy which depends on three complex order parameters: two intraband ones, η_1 and η_2 , and one interband one, $\tilde{\eta}$. This increases the number of possible stable superconducting states, some of them breaking TR symmetry [29–32].

In this paper, we show how the interband pairing affects the topological properties of a two-band SC, which is manifested in a qualitative reconstruction of the energy gap of the Bogoliubov excitations. We focus on two 1D pairing channels, s -wave and d -wave, on a two-dimensional (2D) square lattice and consider both TR-invariant and TR symmetry-breaking superconducting states. The gap functions corresponding to the intraband and interband pairing are introduced using a symmetry-based phenomenological approach. This approach allows one to determine the gap structure, in particular, the location of the gap nodes, even if the microscopic pairing mechanism is not known, and has proved to be very useful in the studies of unconventional fermionic superfluids and superconductors [33,34].

According to the bulk-boundary correspondence principle, changes in the topology of the bulk state are reflected in the

*kirill.samokhin@brocku.ca

Published by the American Physical Society under the terms of the [Creative Commons Attribution 4.0 International license](https://creativecommons.org/licenses/by/4.0/). Further distribution of this work must maintain attribution to the author(s) and the published article's title, journal citation, and DOI.

spectrum of the fermionic modes at the boundary [35,36]. In particular, the boundary modes are expected to be different for nodeless (fully gapped) and nodal (gapless) superconducting states. These boundary modes, also known as the Andreev bound states (ABSs), have been extensively used in experimental probes to identify unconventional pairing states [37,38]. In our paper, we calculate the boundary mode spectrum by solving numerically the Bogoliubov–de Gennes (BdG) equations for a 2D lattice model of a two-band SC, and show how varying the strength of the interband pairing causes the system to undergo a series of topological phase transitions.

The paper is organized as follows: In Sec. II, we derive the possible interband pairing gap functions compatible with s -wave, d_{xy} -wave, and $d_{x^2-y^2}$ -wave intraband pairing, respectively. In Sec. III, we discuss the bulk spectrum and, in particular, the movement of the gap nodes in the Brillouin zone when tuning the interband pairing. In Sec. IV, we numerically compute the edge spectrum of a d_{xy} -wave superconductor with a strip geometry and find a topological phase transition driven by the interband pairing strength. Finally, in Sec. V, we analyze the topological phase found in Sec. IV and calculate the corresponding topological invariant(s).

Throughout the paper we use the units in which $\hbar = 1$, neglecting, in particular, the difference between the quasiparticle wave vector and momentum. Additionally, the lattice constant is set to unity.

II. GAP SYMMETRY: GENERAL CONSIDERATIONS

We focus on a quasi-2D centrosymmetric TR-invariant crystal described by the point group $\mathbb{G} = \mathbf{D}_{4h}$ (however, our results can be straightforwardly generalized to other crystal symmetries); $g \in \mathbb{G}$ is either a proper rotation $R \in SO(3)$ or an improper rotation IR , where I denotes spatial inversion. The electron Bloch states are twofold degenerate at each wave vector $\mathbf{k} = (k_x, k_y)$ due to the combined symmetry KI , called conjugation [39]. We use the index n to label the bands and an additional Kramers index s to distinguish two orthonormal conjugate states within the same band.

We further assume that only two bands $n = 1, 2$ cross the chemical potential and participate in superconductivity, and also that, despite the presence of the electron-lattice spin-orbit coupling, the Bloch states in both bands transform under the point-group operations and TR in the same way as the pure spin-1/2 states. Then, the conjugacy index $s = \uparrow, \downarrow$ can be regarded as a pseudospin projection transforming under time reversal as $K|\mathbf{k}, n \uparrow\rangle = |-\mathbf{k}, n \downarrow\rangle$ and $K|\mathbf{k}, n \downarrow\rangle = -|-\mathbf{k}, n \uparrow\rangle$, and we have

$$g|\mathbf{k}, ns\rangle = \sum_{s'} |g\mathbf{k}, ns'\rangle D_{s's}^{(1/2)}(R). \quad (1)$$

Here, $\hat{D}^{(1/2)}(R)$ is the spin-1/2 representation of R . In other words, we assume that both bands correspond to the double-valued irreducible representation (irrep) Γ_6^+ of \mathbf{D}_{4h} [40]. The assumption (1), which is widely used in the theory of unconventional superconductivity [41], can be relaxed and the band symmetries corresponding to other, non-pseudo-spin, double-valued irreps of the point group can be considered, with important consequences for the superconducting gap structure [42,43].

The superconducting system is described by the Hamiltonian

$$\mathcal{H} = \mathcal{H}_0 + \mathcal{H}_{SC}, \quad (2)$$

where \mathcal{H}_0 is the single-particle Hamiltonian and \mathcal{H}_{SC} the attractive two-particle interaction Hamiltonian within a mean-field approximation. The single-particle Hamiltonian is given by

$$\mathcal{H}_0 = \sum_{kns} \xi_n(\mathbf{k}) c_{k,ns}^\dagger c_{k,ns},$$

where $\xi_n(\mathbf{k}) = \xi_n(-\mathbf{k})$ are the band dispersions counted from the chemical potential, so that $\xi_1(\mathbf{k}) < \xi_2(\mathbf{k})$ for all \mathbf{k} between the two Fermi surfaces. The superconducting mean-field pairing Hamiltonian can be represented in the following form:

$$\mathcal{H}_{SC} = \frac{1}{2} \sum_{knn'ss'} \Delta_{nn'ss'}(\mathbf{k}) c_{k,ns}^\dagger \tilde{c}_{k,n's'}^\dagger + \text{H.c.}, \quad (3)$$

where

$$\tilde{c}_{k,ns}^\dagger \equiv K c_{k,ns}^\dagger K^{-1} = (i\sigma_2)_{s\bar{s}} c_{-\mathbf{k},n\bar{s}}^\dagger$$

are the creation operators in the time-reversed states (\bar{s} flips s).

The intraband pairing in the n th band is described by $\hat{\Delta}_{nn}$, whereas $\hat{\Delta}_{12}$ and $\hat{\Delta}_{21}$ describe the pairing of quasiparticles from different bands (the interband pairing). In order to have a nonvanishing interband pairing in a BCS-like model, one has to assume that the pairing interaction shells near the Fermi surfaces, which are defined by $|\xi_1|, |\xi_2| \leq \epsilon_c$, overlap, i.e., the pairing energy cutoff ϵ_c exceeds the typical band splitting \mathcal{E}_b . We do not attempt to derive the pairing Hamiltonian (3) from any microscopic model and regard the gap functions as phenomenological parameters. The strength of the interband vs intraband pairing is model dependent [44], with the extreme case of a purely interband pairing discussed, e.g., in Ref. [22] in the context of iron-pnictide superconductors.

Note that the gap functions $\hat{\Delta}_{nn'}(\mathbf{k})$ are defined in Eq. (3) as the measures of the pairing between the quasiparticles in the states $|\mathbf{k}, ns\rangle$ and $K|\mathbf{k}, n's'\rangle$, not between $|\mathbf{k}, ns\rangle$ and $|-\mathbf{k}, n's'\rangle$. We neglect the possibility of a nonzero center-of-mass momentum of the interband pairs, which may lead to a nonuniform SC state of the Fulde-Ferrell-Larkin-Ovchinnikov (FFLO) type [45,46]. One can show [32] that the FFLO instability is generally suppressed due to the hybridization of the intraband and interband condensates.

The gap function matrices can be represented as

$$\hat{\Delta}_{nn'}(\mathbf{k}) = \psi_{nn'}(\mathbf{k}) \hat{\sigma}_0 + \mathbf{d}_{nn'}(\mathbf{k}) \cdot \hat{\boldsymbol{\sigma}}, \quad (4)$$

where $\hat{\sigma}_0$ and $\hat{\boldsymbol{\sigma}}$ are respectively the unit matrix and the Pauli matrices in the pseudospin space, then Eq. (3) takes the form

$$\begin{aligned} \mathcal{H}_{SC} = & \frac{1}{2} \sum_{knn'ss'} [\psi_{nn'}(\mathbf{k})(i\sigma_2)_{ss'} \\ & + \mathbf{d}_{nn'}(\mathbf{k})(i\sigma_2)_{s\bar{s}'}] c_{k,ns}^\dagger c_{-\mathbf{k},n's'}^\dagger + \text{H.c.} \end{aligned}$$

Therefore, $\psi_{nn'}$ can be interpreted as the pseudospin-singlet component of the gap function and $\mathbf{d}_{nn'}$ as the pseudospin-triplet component. It follows from the anticommutation of the

fermionic operators that $\psi_{n'n}(\mathbf{k}) = \psi_{n'n}(-\mathbf{k})$ and $\mathbf{d}_{n'n}(\mathbf{k}) = -\mathbf{d}_{n'n}(-\mathbf{k})$.

Additional symmetry constraints on the gap functions are obtained by looking at the transformation of the mean-field Hamiltonian (3) under the point-group operations and TR. Different pairing channels correspond to different single-valued irreps γ of \mathbb{G} . For $\mathbb{G} = \mathbf{D}_{4h}$, we consider only three even-parity pairing channels: the s -wave pairing which corresponds to the trivial irrep A_{1g} and the d -wave pairing which corresponds to either B_{1g} ($d_{x^2-y^2}$ pairing) or B_{2g} (d_{xy} pairing). It follows from Eq. (1) that if the pairing is described by a 1D irrep, then the gap functions satisfy the following constraints:

$$\hat{D}^{(1/2)}(R)\hat{\Delta}_{n'n'}(g^{-1}\mathbf{k})\hat{D}^{(1/2)\dagger}(R) = \chi_\gamma(g)\hat{\Delta}_{n'n'}(\mathbf{k}), \quad (5)$$

where $\chi_\gamma(g)$ are the group characters of the irrep γ . In particular, setting $g = I$, we have $\hat{\Delta}_{n'n'}(-\mathbf{k}) = \hat{\Delta}_{n'n'}(\mathbf{k})$ because $\chi_\gamma(I) = 1$ in the even irreps. The response of the gap functions to TR is given by $\hat{\Delta}_{n'n'}(\mathbf{k}) \rightarrow \hat{\Delta}_{n'n'}^\dagger(\mathbf{k})$.

Next, we introduce the order parameter components $\eta_{n'n'}$ and represent the gap functions in the form $\hat{\Delta}_{n'n'}(\mathbf{k}) = \eta_{n'n'}\hat{\phi}_{n'n'}(\mathbf{k})$. The basis functions $\hat{\phi}_{n'n'}$ which determine the momentum dependence of the gap—in particular, the location of the gap nodes—are 2×2 matrices in the pseudospin space, which satisfy the point-group constraint Eq. (5) and can have singlet and triplet components similar to Eq. (4). Note that $\hat{\phi}_{21}(\mathbf{k}) = \hat{\sigma}_2\hat{\phi}_{12}^\dagger(-\mathbf{k})\hat{\sigma}_2$ due to the anticommutation of the fermionic operators. Regarding the constraint imposed by TR, one can prove that the basis functions can be chosen to satisfy $\hat{\phi}_{n'n'}(\mathbf{k}) = \hat{\phi}_{n'n'}^\dagger(\mathbf{k})$.

Denoting the intraband order parameters as $\eta_n \equiv \eta_{nn}$ and observing that the interband gap functions $\hat{\Delta}_{12}$ and $\hat{\Delta}_{21}$ are not independent and characterized by the same order parameter $\tilde{\eta} \equiv \eta_{12} = \eta_{21}$, we finally obtain

$$\begin{aligned} \hat{\Delta}_{11}(\mathbf{k}) &= \eta_1\alpha_1(\mathbf{k})\hat{\sigma}_0 = \psi_1(\mathbf{k})\hat{\sigma}_0, \\ \hat{\Delta}_{22}(\mathbf{k}) &= \eta_2\alpha_2(\mathbf{k})\hat{\sigma}_0 = \psi_2(\mathbf{k})\hat{\sigma}_0, \\ \hat{\Delta}_{12}(\mathbf{k}) &= \tilde{\eta}[\tilde{\alpha}(\mathbf{k})\hat{\sigma}_0 + i\tilde{\beta}(\mathbf{k}) \cdot \hat{\sigma}], \\ \hat{\Delta}_{21}(\mathbf{k}) &= \tilde{\eta}[\tilde{\alpha}(\mathbf{k})\hat{\sigma}_0 - i\tilde{\beta}(\mathbf{k}) \cdot \hat{\sigma}]. \end{aligned} \quad (6)$$

Here α_1 , α_2 , $\tilde{\alpha}$, and $\tilde{\beta}$ are real even functions of \mathbf{k} . The intraband pairing in the even channels is purely singlet; the interband pairing has both singlet and triplet components. The Pauli principle is not violated because the exchange of electrons in an interband pair involves not only the reversal of their momenta but also the exchange of the band indices.

Our system is characterized by three order parameter components η_1 , η_2 , and $\tilde{\eta}$ which can be found by minimizing the Ginzburg-Landau free energy [32]. It is easy to show that the action of TR on the order parameter components η_1 , η_2 , and $\tilde{\eta}$ is equivalent to complex conjugation (see Appendix A). One can always choose one of the components, say $\tilde{\eta}$, to be real and positive; then, η_1 and η_2 are either both real (positive or negative), which corresponds to a TR-invariant superconducting state, or have complex phases other than 0 or π , which corresponds to a TR symmetry-breaking superconducting state (see Appendix B).

The point-group constraints on the basis functions take the following form:

$$\begin{aligned} \alpha_n(g^{-1}\mathbf{k}) &= \chi_\gamma(g)\alpha_n(\mathbf{k}), \\ \tilde{\alpha}(g^{-1}\mathbf{k}) &= \chi_\gamma(g)\tilde{\alpha}(\mathbf{k}), \\ R(g)\tilde{\beta}(g^{-1}\mathbf{k}) &= \chi_\gamma(g)\tilde{\beta}(\mathbf{k}), \end{aligned} \quad (7)$$

where $R(g)$ denotes the rotational part of g . Below we are looking for real and even-in- \mathbf{k} solutions of these equations, for $g = C_{4z}$ and C_{2y} (the two rotational generators of the group \mathbf{D}_{4h}). To facilitate the numerical analysis later in the paper, the solutions are expressed in terms of the lattice-adapted basis functions of the even 1D irreps of \mathbf{D}_{4h} , namely,

$$\begin{aligned} f_{A_{1g}}(\mathbf{k}) &= 1, \\ f_{A_{2g}}(\mathbf{k}) &= \sin(k_x)\sin(k_y)[\cos(k_x) - \cos(k_y)], \\ f_{B_{1g}}(\mathbf{k}) &= \cos(k_x) - \cos(k_y), \\ f_{B_{2g}}(\mathbf{k}) &= \sin(k_x)\sin(k_y). \end{aligned}$$

For analytical calculations, it is more convenient to use the expressions that depend only on the direction of the wave vector in the xy plane:

$$\begin{aligned} f_{A_{1g}}(\mathbf{k}) &= 1, \\ f_{A_{2g}}(\mathbf{k}) &= \sin(4\theta), \\ f_{B_{1g}}(\mathbf{k}) &= \cos(2\theta), \\ f_{B_{2g}}(\mathbf{k}) &= \sin(2\theta), \end{aligned} \quad (8)$$

where $\mathbf{k} = k(\cos\theta, \sin\theta)$.

A. s -wave pairing

For $\gamma = A_{1g}$, the simplest singlet solutions of the symmetry constraints (7) are given by $\alpha_1(\mathbf{k}) = \alpha_2(\mathbf{k}) = \tilde{\alpha}(\mathbf{k}) = f_{A_{1g}} = 1$. Since C_{2z} is a symmetry element, for the triplet interband component we have $\tilde{\beta}(\mathbf{k}) = C_{2z}\tilde{\beta}(C_{2z}^{-1}\mathbf{k}) = C_{2z}\tilde{\beta}(-\mathbf{k}) = C_{2z}\tilde{\beta}(\mathbf{k})$; therefore, $\tilde{\beta}_1 = \tilde{\beta}_2 = 0$. It is easy to show that $\tilde{\beta}_3 \propto f_{A_{2g}}$: since \hat{z} and $\hat{\sigma}_3$ also correspond to A_{2g} , $\tilde{\beta}_3\hat{\sigma}_3$ indeed corresponds to $A_{2g} \times A_{2g} = A_{1g}$. Collecting everything together, we arrive at the following expressions for the gap functions:

$$\begin{aligned} \hat{\Delta}_{11}(\mathbf{k}) &= \eta_1\hat{\sigma}_0, \\ \hat{\Delta}_{22}(\mathbf{k}) &= \eta_2\hat{\sigma}_0, \\ \hat{\Delta}_{12}(\mathbf{k}) &= \tilde{\eta}[\hat{\sigma}_0 + i\rho f_{A_{2g}}(\mathbf{k})\hat{\sigma}_3], \\ \hat{\Delta}_{21}(\mathbf{k}) &= \tilde{\eta}[\hat{\sigma}_0 - i\rho f_{A_{2g}}(\mathbf{k})\hat{\sigma}_3], \end{aligned} \quad (9)$$

where ρ is a real parameter. One can say that the interband gap functions in the A_{1g} channel correspond to an $s + ig$ pairing, with the understanding that the s and g components have a different pseudospin structure.

B. d -wave pairing

The singlet components of the gap functions can be chosen in the standard form: $\alpha_1(\mathbf{k}) = \alpha_2(\mathbf{k}) = \tilde{\alpha}(\mathbf{k}) = f_{B_{1g}}(\mathbf{k})$ or $f_{B_{2g}}(\mathbf{k})$, for $d_{x^2-y^2}$ - or d_{xy} -wave pairing, respectively. For the same reason as in the s -wave case, $\tilde{\beta}_1 = \tilde{\beta}_2 = 0$, and, using

$B_{2g} \times A_{2g} = B_{1g}$ and $B_{2g} \times A_{2g} = B_{1g}$, we obtain

$$\begin{aligned}\hat{\Delta}_{11}(\mathbf{k}) &= \eta_1 f_{B_{1g}}(\mathbf{k}) \hat{\sigma}_0, \\ \hat{\Delta}_{22}(\mathbf{k}) &= \eta_2 f_{B_{1g}}(\mathbf{k}) \hat{\sigma}_0, \\ \hat{\Delta}_{12}(\mathbf{k}) &= \tilde{\eta} [f_{B_{1g}}(\mathbf{k}) \hat{\sigma}_0 + i\rho f_{B_{2g}}(\mathbf{k}) \hat{\sigma}_3], \\ \hat{\Delta}_{21}(\mathbf{k}) &= \tilde{\eta} [f_{B_{1g}}(\mathbf{k}) \hat{\sigma}_0 - i\rho f_{B_{2g}}(\mathbf{k}) \hat{\sigma}_3],\end{aligned}\quad (10)$$

for the $d_{x^2-y^2}$ -wave pairing and

$$\begin{aligned}\hat{\Delta}_{11}(\mathbf{k}) &= \eta_1 f_{B_{2g}}(\mathbf{k}) \hat{\sigma}_0, \\ \hat{\Delta}_{22}(\mathbf{k}) &= \eta_2 f_{B_{2g}}(\mathbf{k}) \hat{\sigma}_0, \\ \hat{\Delta}_{12}(\mathbf{k}) &= \tilde{\eta} [f_{B_{2g}}(\mathbf{k}) \hat{\sigma}_0 + i\rho f_{B_{1g}}(\mathbf{k}) \hat{\sigma}_3], \\ \hat{\Delta}_{21}(\mathbf{k}) &= \tilde{\eta} [f_{B_{2g}}(\mathbf{k}) \hat{\sigma}_0 - i\rho f_{B_{1g}}(\mathbf{k}) \hat{\sigma}_3],\end{aligned}\quad (11)$$

for the d_{xy} -wave pairing. In both cases, ρ is a real parameter.

We would like to add two comments about the structure of the interband gap functions. First, the momentum dependence of their singlet and triplet components corresponds to different even irreps of the point group (for instance, in the case of d_{xy} pairing, it is B_{2g} for $\tilde{\alpha}$ and B_{1g} for $\tilde{\beta}_3$). However, the pseudospin also transforms under the point-group operations, in such a way that both $\tilde{\alpha}$ and $\tilde{\beta}_3$ correspond to the same pairing channel. It is in this sense that the interband gap functions in both B_{1g} and B_{2g} channels correspond to a $d + id$ pairing. Second, the singlet components in the interband gap functions in Eqs. (10) and (11) have the same symmetry as in the intraband ones. As seen from Eq. (5), this is a consequence of our assumption that both bands correspond to the same double-valued irrep of \mathbf{D}_{4h} . In general, i.e., for the bands corresponding to different irreps, the symmetry of $\tilde{\alpha}$ may be different from that of α .

III. BOGOLIUBOV SPECTRUM IN THE BULK

The mean-field Hamiltonian (2) can be written in the form

$$\mathcal{H} = \text{const} + \frac{1}{2} \sum_{\mathbf{k}} \mathcal{C}^\dagger(\mathbf{k}) \hat{H}_{\text{BdG}}(\mathbf{k}) \mathcal{C}(\mathbf{k}), \quad (12)$$

where we introduced the Nambu spinor operator

$$\mathcal{C}^\dagger(\mathbf{k}) = (c_{k,1\uparrow}, c_{k,1\downarrow}, \tilde{c}_{k,1\uparrow}^\dagger, \tilde{c}_{k,1\downarrow}^\dagger, c_{k,2\uparrow}, c_{k,2\downarrow}, \tilde{c}_{k,2\uparrow}^\dagger, \tilde{c}_{k,2\downarrow}^\dagger) \quad (13)$$

and the BdG Hamiltonian

$$\hat{H}_{\text{BdG}} = \begin{pmatrix} \xi_1 \hat{\sigma}_0 & \hat{\Delta}_{11} & 0 & \hat{\Delta}_{12} \\ \hat{\Delta}_{11}^\dagger & -\xi_1 \hat{\sigma}_0 & \hat{\Delta}_{21}^\dagger & 0 \\ 0 & \hat{\Delta}_{21} & \xi_2 \hat{\sigma}_0 & \hat{\Delta}_{22} \\ \hat{\Delta}_{12}^\dagger & 0 & \hat{\Delta}_{22}^\dagger & -\xi_2 \hat{\sigma}_0 \end{pmatrix}, \quad (14)$$

which is an 8×8 matrix in the tensor product of the band, Nambu, and pseudospin spaces. The gap functions $\hat{\Delta}_{nn'}(\mathbf{k})$ are given by Eqs. (9), (10), and (11).

The Hamiltonian (14) is even in \mathbf{k} and has the built-in particle-hole symmetry:

$$\hat{H}_{\text{BdG}}(\mathbf{k}) = -\hat{\mathcal{U}}_C^\dagger \hat{H}_{\text{BdG}}^*(-\mathbf{k}) \hat{\mathcal{U}}_C,$$

where

$$\hat{\mathcal{U}}_C = \begin{pmatrix} \hat{\tau}_2 \otimes \hat{\sigma}_2 & 0 \\ 0 & \hat{\tau}_2 \otimes \hat{\sigma}_2 \end{pmatrix}$$

and $\hat{\tau}$ are the Pauli matrices in the Nambu space. Since $\hat{\mathcal{U}}_C^\dagger = \hat{\mathcal{U}}_C$, the Hamiltonian is generically in the tenfold class D [47–49]. The TR action on the Nambu operators (13) is given by $K\mathcal{C}(\mathbf{k})K^{-1} = \hat{\mathcal{U}}_K \mathcal{C}(-\mathbf{k})$, where

$$\hat{\mathcal{U}}_K = \begin{pmatrix} \hat{\tau}_0 \otimes i\hat{\sigma}_2 & 0 \\ 0 & \hat{\tau}_0 \otimes i\hat{\sigma}_2 \end{pmatrix}.$$

Therefore,

$$K : \hat{H}_{\text{BdG}}(\mathbf{k}) \rightarrow \hat{\mathcal{U}}_K^\dagger \hat{H}_{\text{BdG}}^*(-\mathbf{k}) \hat{\mathcal{U}}_K, \quad (15)$$

which is equivalent to replacing $(\eta_1, \eta_2, \tilde{\eta}) \rightarrow (\eta_1^*, \eta_2^*, \tilde{\eta}^*)$. If the superconducting state is TR invariant, i.e., η_1, η_2 , and $\tilde{\eta}$ are all real, then the BdG Hamiltonian satisfies an additional constraint:

$$\hat{H}_{\text{BdG}}(\mathbf{k}) = \hat{\mathcal{U}}_K^\dagger \hat{H}_{\text{BdG}}^*(-\mathbf{k}) \hat{\mathcal{U}}_K.$$

Since $\hat{\mathcal{U}}_K^\dagger = -\hat{\mathcal{U}}_K$, the TR invariant BdG Hamiltonian is in the tenfold class DIII.

For the pairing symmetries we consider, the Hamiltonian (2) is invariant under an arbitrary $U(1)$ pseudospin rotation $c_{kn\uparrow(\downarrow)}^\dagger \rightarrow e^{\mp i\theta/2} c_{kn\uparrow(\downarrow)}^\dagger$, and we have $[\hat{H}_{\text{BdG}}, \hat{\Sigma}_3] = 0$, where $\hat{\Sigma}_3 = \mathbb{1}_{4 \times 4} \otimes \hat{\sigma}_3$. Therefore, Eq. (14) can be represented in the form

$$\hat{H}_{\text{BdG}}(\mathbf{k}) = \hat{H}_\uparrow(\mathbf{k}) \oplus \hat{H}_\downarrow(\mathbf{k}),$$

where the Hamiltonians

$$\hat{H}_{\uparrow(\downarrow)} = \begin{pmatrix} \xi_1 & \eta_1 \alpha_1 & 0 & \tilde{\eta}(\tilde{\alpha} \pm i\tilde{\beta}) \\ \eta_1^* \alpha_1 & -\xi_1 & \tilde{\eta}(\tilde{\alpha} \pm i\tilde{\beta}) & 0 \\ 0 & \tilde{\eta}(\tilde{\alpha} \mp i\tilde{\beta}) & \xi_2 & \eta_2 \alpha_2 \\ \tilde{\eta}(\tilde{\alpha} \mp i\tilde{\beta}) & 0 & \eta_2^* \alpha_2 & -\xi_2 \end{pmatrix} \quad (16)$$

act in the two four-dimensional eigenspaces of $\hat{\Sigma}_3$, corresponding to the two pseudospin projections. In Eq. (16) and everywhere below, we use the notation $\tilde{\beta} = \tilde{\beta}_3$ and the interband order parameter $\tilde{\eta}$ is chosen to be real and positive, but the phases of η_1 and η_2 can be arbitrary.

It follows from Eq. (15) that the pseudospin-resolved Hamiltonians \hat{H}_\uparrow and \hat{H}_\downarrow are transformed into each other by TR:

$$K : \hat{H}_\uparrow(\mathbf{k}) \rightarrow \hat{H}_\downarrow^*(-\mathbf{k}) = \hat{H}_\downarrow(\mathbf{k}). \quad (17)$$

Also, they satisfy the relation $\hat{U}^\dagger \hat{H}_\uparrow^*(\mathbf{k}) \hat{U} = -\hat{H}_\downarrow(\mathbf{k})$, where $\hat{U} = \mathbb{1}_{2 \times 2} \otimes \hat{\tau}_2$. Introducing the magnitude and the phase of the interband gap functions

$$\tilde{\eta}(\tilde{\alpha} + i\tilde{\beta}) \equiv \tilde{\Delta}(\mathbf{k}) = |\tilde{\Delta}(\mathbf{k})| e^{i\tilde{\varphi}(\mathbf{k})}, \quad (18)$$

with $|\tilde{\Delta}(\mathbf{k})| = \tilde{\eta} \tilde{g}(\mathbf{k})$ and $\tilde{g} = \sqrt{\tilde{\alpha}^2 + \tilde{\beta}^2}$, one can see that \hat{H}_\uparrow and \hat{H}_\downarrow are particle-hole symmetric at each \mathbf{k} , in the following sense:

$$\hat{U}_{C,\uparrow(\downarrow)}^\dagger(\mathbf{k}) \hat{H}_{\uparrow(\downarrow)}^*(\mathbf{k}) \hat{U}_{C,\uparrow(\downarrow)}(\mathbf{k}) = -\hat{H}_{\uparrow(\downarrow)}(\mathbf{k})$$

where

$$\hat{U}_{C,\uparrow(\downarrow)} = \begin{pmatrix} e^{\mp i\tilde{\varphi}} \hat{\tau}_2 & 0 \\ 0 & e^{\pm i\tilde{\varphi}} \hat{\tau}_2 \end{pmatrix}.$$

Therefore, \hat{H}_\uparrow and \hat{H}_\downarrow have the same bulk spectrum, which consists of symmetric pairs of eigenstates E and $-E$. Since $\hat{U}_{C,\uparrow(\downarrow)}^\dagger = -\hat{U}_{C,\uparrow(\downarrow)}$, the pseudospin-resolved Hamiltonians \hat{H}_\uparrow and \hat{H}_\downarrow are in the tenfold class C.

The matrices \hat{H}_\uparrow and \hat{H}_\downarrow can be diagonalized analytically (see Appendix C), and we find that the bulk Bogoliubov spectrum consists of four branches $\pm E_\pm$, where

$$E_\pm(\mathbf{k}) = \sqrt{P(\mathbf{k}) \pm \sqrt{P^2(\mathbf{k}) - Q^2(\mathbf{k})}} = E_\pm(-\mathbf{k}). \quad (19)$$

The notations are as follows:

$$P = \frac{1}{2}(\xi_1^2 + |\psi_1|^2 + \xi_2^2 + |\psi_2|^2) + |\tilde{\Delta}|^2,$$

$$Q^2 = r_1^2 + r_2^2 + r_3^2,$$

$\psi_n(\mathbf{k}) = \eta_n \alpha_n(\mathbf{k})$ are the intraband gap functions, and

$$r_1 = \xi_1 \xi_2 - |\psi_1 \psi_2| + |\tilde{\Delta}|^2,$$

$$r_2 = \xi_1 |\psi_2| + \xi_2 |\psi_1|,$$

$$r_3 = \sqrt{2|\tilde{\Delta}|^2[|\psi_1 \psi_2| - \text{Re}(\psi_1 \psi_2)]}.$$

One can show that $P > Q$ in the presence of interband pairing. Therefore, E_+ is strictly greater than E_- at all \mathbf{k} . Each of the four branches $\pm E_\pm$ is twofold degenerate due to pseudospin. In the absence of interband pairing, we set $\tilde{\eta} = 0$ and recover the usual expressions for a two-band superconductor:

$$E_+(\mathbf{k}) = \max\{\epsilon_1(\mathbf{k}), \epsilon_2(\mathbf{k})\},$$

$$E_-(\mathbf{k}) = \min\{\epsilon_1(\mathbf{k}), \epsilon_2(\mathbf{k})\},$$

where $\epsilon_n = \sqrt{\xi_n^2 + |\psi_n|^2}$ is the excitation energy in the n th band.

While the upper Bogoliubov excitation branch E_+ is fully gapped in the superconducting state, the lower branch E_- vanishes at the wave vector \mathbf{k} if

$$r_1(\mathbf{k}) = r_2(\mathbf{k}) = r_3(\mathbf{k}) = 0, \quad (20)$$

in which case $E_-(\mathbf{k})$ and $-E_-(\mathbf{k})$ touch, producing a gap node. In two spatial dimensions, the three real functions $r_{1,2,3}$ cannot simultaneously vanish at the same \mathbf{k} , unless forced to do so by additional symmetries.

Writing the intraband order parameters in the form

$$\eta_1 = |\eta_1| e^{i\varphi_1}, \quad \eta_2 = |\eta_2| e^{i\varphi_2}, \quad (21)$$

we see that r_3 identically vanishes in the states in which $\varphi_1 + \varphi_2 = 0$ or 2π . This happens, in particular, in the TR-invariant states in which η_1 and η_2 are both either real positive or real negative. As shown in Appendix B, the TR-symmetry-breaking states with $\varphi_1 + \varphi_2 = 0$ or 2π are stable only if the system's parameters are fine tuned, the possibility that can be neglected. In a generic state with the interband pairing, i.e., when $\tilde{\eta} \neq 0$ and $\varphi_1 + \varphi_2 \neq 0$ or 2π , $r_3(\mathbf{k}) = 0$ only if $\psi_1(\mathbf{k}) = 0$ or $\psi_2(\mathbf{k}) = 0$. In the s -wave case, this can only happen accidentally and is neglected. In contrast, the d -wave intraband gap functions, and therefore r_3 , vanish along the high-symmetry directions for symmetry reasons. Thus, there

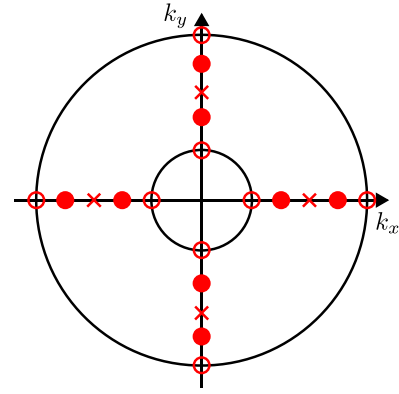


FIG. 1. Schematic illustration of the nodal behavior in the toy model of the generic d_{xy} -wave case (Sec. III B). Empty red dots: high-symmetry nodes without interband pairing $\tilde{\eta} = 0$. Filled red dots: high-symmetry nodes at small interband pairing $0 < \tilde{\eta} < \tilde{\eta}_c$ [see Eq. (26)]. Red crosses: annihilation of high-symmetry nodes at interband pairing $\tilde{\eta} = \tilde{\eta}_c$.

exist four classes of the stable bulk nodal structures, which are studied below.

A. Generic s -wave pairing

In this case, the phases of η_1 and η_2 take any values, except $\varphi_1 = \varphi_2 = 0$ or π . The TR invariant states in which η_1 and η_2 are real but have opposite signs are also included here. Since r_3 is nonzero at all \mathbf{k} , the s -wave superconducting state is fully gapped, regardless of the strength of the interband pairing.

B. Generic d -wave pairing

For concreteness, let us consider the evolution of the nodal structure in the d_{xy} -wave case (for the $d_{x^2-y^2}$ -wave pairing, the nodes are just rotated by $\pi/4$). In the absence of the interband pairing, r_3 identically vanishes and the point gap nodes are located where $\xi_1 = \psi_1 = 0$ or $\xi_2 = \psi_2 = 0$, i.e., at the intersections of the axes of the 2D Brillouin zone with the Fermi surfaces.

In the presence of the interband pairing and for generic phases of η_1 and η_2 , r_3 only vanishes along the axes $k_x = 0$ and $k_y = 0$ for symmetry reasons. Moreover, r_2 is also zero there and the only remaining gap node condition, Eq. (20), takes the following form:

$$\xi_1 \xi_2 = -\tilde{\eta}^2 \tilde{g}^2 \quad (22)$$

along the $k_x = 0$ or $k_y = 0$ lines. As $\tilde{\eta}$ increases, the nodes remain on the high-symmetry axes, but move into the “interband space,” where $\xi_1 < 0$ and $\xi_2 > 0$ (recall that we assume $\xi_1 < \xi_2$). Eventually, at a sufficiently strong interband pairing, the nodes merge and annihilate each other, which marks the transition into a fully gapped bulk phase, as shown in Fig. 1. Annihilating nodes were also found in Ref. [50], in a model of a TR-invariant SC with a $d_{x^2-y^2}$ -wave intraband pairing and d_{xy} -wave interband pairing.

The evolution of the gap structure can be studied analytically using a simple model with two parabolic electronlike

bands:

$$\xi_{1(2)}(\mathbf{k}) = \xi(\mathbf{k}) \mp \frac{\mathcal{E}_b}{2}, \quad \xi(\mathbf{k}) = \frac{k^2 - k_0^2}{2m}, \quad (23)$$

where $\mathcal{E}_b > 0$ is the band splitting, in which the two Fermi surfaces are circles of radii $k_{F,1(2)} = k_0\sqrt{1 \pm m\mathcal{E}_b/k_0^2}$. We use the following gap symmetry factors:

$$\begin{aligned} \alpha_1 = \alpha_2 = \tilde{\alpha} &= \sin(2\theta), \\ \tilde{\beta} &= \rho \cos(2\theta) \end{aligned} \quad (24)$$

[see Eqs. (11) and (8)]. The gap node equation (22) becomes

$$\xi^2 = \left(\frac{\mathcal{E}_b}{2}\right)^2 - \tilde{\eta}^2 \rho^2,$$

along the axes of the momentum space. Taking, for instance, the $\theta = 0$ axis, at $\tilde{\eta} = 0$ the two nodes are located on the Fermi surfaces, at $\mathbf{k} = k_{F,1}\hat{x}$ and $k_{F,2}\hat{x}$. As $\tilde{\eta}$ increases, the nodes move towards each other, to $\mathbf{k} = k_1\hat{x}$ and $k_2\hat{x}$, where

$$k_{1,2} = k_0 \left[1 \pm \frac{2m}{k_0^2} \sqrt{\left(\frac{\mathcal{E}_b}{2}\right)^2 - \tilde{\eta}^2 \rho^2} \right]^{1/2}. \quad (25)$$

Finally, when the interband order parameter $\tilde{\eta}$ reaches the critical value

$$\tilde{\eta}_c = \frac{\mathcal{E}_b}{2|\rho|}, \quad (26)$$

the nodes merge at $\mathbf{k} = k_0\hat{x}$ and “annihilate” each other. At stronger interband pairing, our d_{xy} -wave superconductor is fully gapped.

Note that the disappearance of the nodes happens only if $\rho \neq 0$, i.e., when the interband gap functions contain the triplet component with the $d_{x^2-y^2}$ -wave-like momentum dependence. The singlet components of both the intraband and interband gaps have the same symmetry and vanish along the high-symmetry axes, whereas the interband triplet component does not vanish there and controls the behavior of the nodes.

C. s -wave pairing, $\varphi_1 = \varphi_2 = 0$ or π

In this TR invariant state, r_3 is identically zero everywhere, but we still need to solve the remaining equations $r_1 = 0$ and $r_2 = 0$. Assuming, without loss of generality, the same intraband symmetry factors in both bands, $\alpha_1(\mathbf{k}) = \alpha_2(\mathbf{k}) = \alpha(\mathbf{k})$, the equation $r_2 = 0$ takes the form $|\alpha|(\xi_1|\eta_2| + \xi_2|\eta_1|) = 0$. One way to satisfy this is to put $\alpha = 0$, but that does not happen in the s -wave case, whereas in the d -wave case that can happen only along the high-symmetry lines, which was already considered in Sec. III B. Therefore, if we look for the gap nodes away from the high-symmetry axes, then we need to solve the following two equations:

$$\begin{aligned} |\xi_1(\mathbf{k})\xi_2(\mathbf{k})| &= \tilde{\eta}^2 \tilde{\rho}^2(\mathbf{k}) - |\eta_1\eta_2|\alpha^2(\mathbf{k}), \\ 0 &= \xi_1(\mathbf{k})|\eta_2| + \xi_2(\mathbf{k})|\eta_1|. \end{aligned} \quad (27)$$

Note that the second equation can have solutions only between the two Fermi surfaces, where $\xi_1 < 0$ and $\xi_2 > 0$, i.e., $\xi_1\xi_2 = -|\xi_1\xi_2|$. If the interband pairing is sufficiently strong, so that the right-hand side of the first equation is positive,

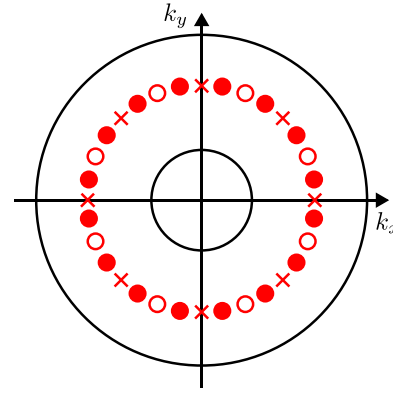


FIG. 2. Schematic illustration of the nodal behavior in the toy model of the exceptional s -wave case (Sec. III C). Empty red dots: stray nodes at interband pairing $\tilde{\eta} = \tilde{\eta}_{c,1}$ [see Eq. (29)]. Filled red dots: stray nodes at interband pairing $\tilde{\eta}_{c,1} < \tilde{\eta} < \tilde{\eta}_{c,2}$ [see Eq. (30)]. Red crosses: annihilation of stray nodes at interband pairing $\tilde{\eta} = \tilde{\eta}_{c,2}$.

then Eq. (27) defines two lines between the Fermi surfaces. The intersections of these lines, if they exist, correspond to accidental point nodes in the excitation spectrum.

To illustrate these points for the s -wave pairing, we use the band structure model Eq. (23), with the following angular dependence of the gap functions:

$$\alpha = \tilde{\alpha} = 1, \quad \tilde{\beta} = \rho \sin(4\theta)$$

[see Eqs. (9) and (8)]. Solving Eq. (27), we obtain that the accidental nodes are located on the circle of the radius

$$K = k_0 \sqrt{1 + \zeta \frac{m\mathcal{E}_b}{k_0^2}}, \quad k_{F,2} < K < k_{F,1}, \quad (28)$$

where

$$\zeta = \frac{|\eta_2| - |\eta_1|}{|\eta_2| + |\eta_1|}, \quad |\zeta| < 1,$$

at the angles found from the equation

$$\tilde{\eta}^2 [1 + \rho^2 \sin^2(4\theta)] - |\eta_1\eta_2| = (1 - \zeta^2) \left(\frac{\mathcal{E}_b}{2}\right)^2.$$

In the absence of the interband pairing, this last equation does not have any solutions. As $\tilde{\eta}$ increases and reaches

$$\tilde{\eta}_{c,1} = \sqrt{\frac{|\eta_1\eta_2|}{1 + \rho^2}} \sqrt{1 + \left(\frac{\mathcal{E}_b}{|\eta_1| + |\eta_2|}\right)^2}, \quad (29)$$

the nodes emerge in pairs, first at the angles given by $\theta = \pi/8, 3\pi/8, \dots$. As the interband pairing further increases, the nodes split and move along the circle defined by Eq. (28) towards the angles $\theta = 0, \pi/4, \dots$, where they finally merge and disappear at

$$\tilde{\eta}_{c,2} = \sqrt{1 + \rho^2} \tilde{\eta}_{c,1}. \quad (30)$$

These changes in the gap structure are shown in Fig. 2. The superconducting state is fully gapped at $\tilde{\eta} < \tilde{\eta}_{c,1}$ and at $\tilde{\eta} > \tilde{\eta}_{c,2}$.

Note that the gap nodes appear for the s -wave pairing in the model (23) only if $\rho \neq 0$, i.e., when the interband gap

functions contain the “triplet” component with an anisotropic, g -wave-like momentum dependence. Although these nodes are topologically unstable, since any deviation from the condition $\varphi_1 = \varphi_2 = 0$ or π will remove them, they are protected by TR symmetry. Accidental nodes may also be produced in a more general model in which either the band dispersions or the singlet parts of the gap functions are anisotropic. We do not investigate this possibility here.

D. d -wave pairing, $\varphi_1 = \varphi_2 = 0$ or π

The difference from the generic d -wave case is that r_3 now vanishes everywhere, which makes it possible for additional gap nodes to appear away from the high-symmetry lines. Repeating the reasoning from Sec. III C, we find that there are two types of nodes: the “high-symmetry” ones, which are located where $\alpha(\mathbf{k}) = 0$, and also the “stray” ones, which correspond to the solutions of Eq. (27).

To develop some analytical insight, we again assume a d_{xy} -wave pairing and use the parabolic bands (23), with the symmetry factors given by Eq. (24). We obtain that the stray nodes are located on the circle defined by Eq. (28), at the angles determined by the equation

$$(1 - \zeta^2) \left(\frac{\mathcal{E}_b}{2} \right)^2 = \tilde{\eta}^2 [\sin^2(2\theta) + \rho^2 \cos^2(2\theta)] - |\eta_1 \eta_2| \sin^2(2\theta). \quad (31)$$

At $\tilde{\eta} = 0$, this equation has no solutions. To illustrate the different scenarios of how the stray nodes are created and destroyed by increasing the interband pairing strength, we solve Eq. (31) in three cases, for $\rho = 0$, $|\rho| \gg 1$, and $\rho = 1$.

At $\rho = 0$, which corresponds to the absence of the triplet $d_{x^2-y^2}$ component in the interband gap functions, the stray nodes appear in pairs at $\theta = \pi/4, 3\pi/4, \dots$ when $\tilde{\eta}$ reaches the critical value

$$\tilde{\eta}_{c,1} = \sqrt{|\eta_1 \eta_2|} \sqrt{1 + \left(\frac{\mathcal{E}_b}{|\eta_1| + |\eta_2|} \right)^2}.$$

As the interband pairing strength further increases, the nodes split and move away from each other, staying on the circle (28) and asymptotically approaching the axes $\theta = 0, \pi/2, \dots$. Since at $\rho = 0$ both the intraband and interband gap functions vanish along the axes, the high-symmetry nodes are not affected by $\tilde{\eta}$, i.e., always remain at the intersections of the two Fermi surfaces with the lines $k_x = 0$ and $k_y = 0$. Note that, in contrast to the generic d -wave pairing considered in Sec. III B, one does not need the triplet interband component to control the stray nodes. The reason is that the stray nodes are located away from the high-symmetry axes, where the singlet interband components are nonzero.

At $|\rho| \gg 1$, which corresponds to the triplet $d_{x^2-y^2}$ component dominating the interband gap functions, the stray nodes appear at $\theta = 0, \pi/2, \dots$ when the interband pairing strength reaches

$$\tilde{\eta}_{c,1} = \frac{\sqrt{|\eta_1 \eta_2|}}{|\rho|(|\eta_1| + |\eta_2|)} \mathcal{E}_b.$$

At this point they “peel off” in pairs from the high-symmetry nodes and, as $\tilde{\eta}$ increases, move along the circle (28) towards

the diagonals. Whereas the high-symmetry nodes annihilate each other at $\tilde{\eta}_c > \tilde{\eta}_{c,1}$ [see Eq. (26)], the stray nodes survive in the limit $\tilde{\eta} \gg \tilde{\eta}_{c,1}$, asymptotically approaching the axes $\theta = \pi/4, 3\pi/4, \dots$.

To see what happens in the general case, when both the singlet (d_{xy}) and the triplet ($d_{x^2-y^2}$) components are present in the interband gap functions, we set $\rho = 1$. Then, the solutions of Eq. (31) exist only if $\tilde{\eta}_{c,1} \leq \tilde{\eta} \leq \tilde{\eta}_{c,2}$, where

$$\tilde{\eta}_{c,1} = \frac{\sqrt{|\eta_1 \eta_2|}}{|\eta_1| + |\eta_2|} \mathcal{E}_b, \quad (32)$$

and

$$\tilde{\eta}_{c,2} = \sqrt{|\eta_1 \eta_2|} \sqrt{1 + \left(\frac{\mathcal{E}_b}{|\eta_1| + |\eta_2|} \right)^2}. \quad (33)$$

As $\tilde{\eta}$ increases, the stray nodes first appear on the axes, i.e., at $\theta = 0, \pi/2, \dots$, where they peel off in pairs from the high-symmetry nodes, then move towards $\theta = \pi/4, 3\pi/4, \dots$, where they eventually merge and annihilate each other. Note that $\tilde{\eta}_{c,1}$ is less than the critical strength of the interband pairing at which the high-symmetry nodes disappear [see Eq. (26)]. Therefore, there is an interval of $\tilde{\eta}$, in which the stray nodes coexist with the high-symmetry ones, so that there are 16 nodes altogether (eight of each type), all located between the Fermi surfaces, as shown in Fig. 3. Similar behavior of the nodes was also found in a different model in Ref. [51], in which the interband pairing in a TR invariant d -wave state is controlled by the interorbital SO coupling. In contrast to the limiting cases of $\rho = 0$ and $\rho \gg 1$, in which $\tilde{\eta}_{c,2} = \infty$ and the stray nodes survive the strong interband pairing, in the general case all nodes eventually disappear as $\tilde{\eta}$ increases.

The stray nodes are accidental, in the sense that they are not protected by the crystal symmetry. In order to destroy them, one has to tune the intraband order parameter phases out of the TR-invariance condition $\varphi_1 = \varphi_2 = 0$ or π . However, this condition always corresponds to a critical point of the free energy (see Appendix B), and if this critical point is a minimum, then the state is stable. Therefore, the stray nodes are protected by the TR symmetry.

E. Summary

The effect of the interband pairing on the energy gap nodes in the bulk is fundamentally different in the four cases discussed in this section. The least interesting case is the generic s -wave state, which is fully gapped at $\tilde{\eta} = 0$ and remains so as $\tilde{\eta}$ increases. This state is topologically trivial and does not support zero-energy boundary modes.

In the TR-invariant s -wave state with $\varphi_1 = \varphi_2 = 0$ or π , a sufficiently strong interband pairing can create and then destroy again point nodes between the Fermi surfaces. The critical values of $\tilde{\eta}$ separating the gapped and gapless phases, as well as the locations of the nodes, are model dependent.

In the generic d -wave state, the nodes are located only along the high-symmetry lines. As $\tilde{\eta}$ increases, these nodes leave the Fermi surfaces, move towards each other into the interband space, and merge and disappear at $\tilde{\eta} = \tilde{\eta}_c$. The gapless and gapped phases separated by $\tilde{\eta}_c$ are expected to be topologically different, which is confirmed in Secs. IV and V below.

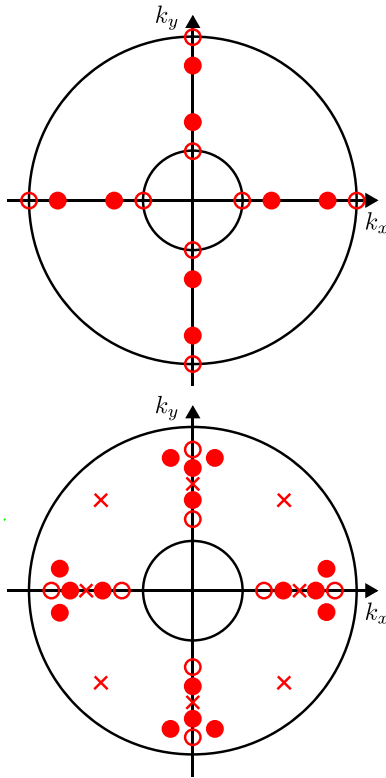


FIG. 3. Schematic illustration of the nodal behavior in the toy model of the exceptional d_{xy} -wave case (Sec. III D). Top: Empty red dots, high-symmetry nodes without interband pairing $\tilde{\eta} = 0$; filled red dots, high-symmetry nodes at small interband pairing $0 < \tilde{\eta} < \tilde{\eta}_{c,1}$ [see Eq. (32)]. Bottom: Empty red dots, high-symmetry nodes at interband pairing $\tilde{\eta} \lesssim \tilde{\eta}_{c,1}$; filled red dots, high-symmetry nodes (along the main axes) and stray nodes (off the main axes) at interband pairing $\tilde{\eta}_{c,1} < \tilde{\eta} < \tilde{\eta}_{c,2}$ [see Eq. (33)]; red crosses, annihilation of high-symmetry nodes (along the main axes) at interband pairing $\tilde{\eta} = \tilde{\eta}_c$ and annihilation of stray nodes (off the main axes) at interband pairing $\tilde{\eta} = \tilde{\eta}_{c,2}$ ($\tilde{\eta}_c < \tilde{\eta}_{c,2}$).

The TR-invariant d -wave state with $\varphi_1 = \varphi_2 = 0$ or π exhibits the most complex behavior. In this case, the nodes along the high-symmetry lines can coexist with the additional (stray) nodes in the interband space, whose number and locations are model dependent. As the interband pairing increases, the two families of nodes evolve as the system passes through a series of transitions characterized by the creation and destruction of the pairs of nodes. Across these transitions, the topological charges of the nodes are conserved (see Sec. V A). Eventually, at a sufficiently large $\tilde{\eta}$, all the nodes will have pairwise collided and annihilated each other, so that the superconducting state will be fully gapped.

IV. BOUNDARY MODES

Having discussed the bulk properties of the different superconducting phases in Sec. III, we turn our attention towards the boundaries of the material. We consider a strip geometry: the system is infinitely extending along the x direction, but has a finite width along the y direction. To formulate the lattice model, we assume N_x (N_y) lattice sites with periodic (open)

boundary conditions along the x (y) direction. As a result, the system effectively possesses two infinitely extended edges parallel to the x axis.

The bulk band structure is described by

$$\xi_n(\mathbf{k}) = -2t_n[\cos(k_x) + \cos(k_y)] - 4t'_n \cos(k_x) \cos(k_y) - \mu,$$

where μ is the chemical potential, t_n is the nearest-, and t'_n is the next-nearest-neighbor hopping amplitude in the n th band. Superconductivity is either of s - or d_{xy} -wave type, given by Eqs. (9) and (11), respectively; for $d_{x^2-y^2}$ -wave superconductivity, we would consider edges rotated by $\pi/4$. The total bulk Hamiltonian of the lattice model is described by Eq. (2).

The formal description of the superconducting strip system follows Ref. [52]. The momentum component k_y is not a good quantum number, because translation symmetry is broken along the y direction. To account for this, we only consider the momentum representation $k \equiv k_x$ along the x direction, while we keep the real space representation $i \equiv i_y$ along the y direction. Assuming a sufficiently wide strip, the superconducting gap is approximately constant along the y direction and we neglect any potential surface effects causing the order parameter to be spatially deformed close to the edges. The order parameters η_1 , η_2 , and $\tilde{\eta}$ are not computed self-consistently, but set to their respective bulk values.

Similar to Eq. (12), the total mean-field Hamiltonian is of the form

$$\mathcal{H} = \text{const} + \frac{1}{2} \sum_k C^\dagger(k) \hat{H}_{\text{BdG}}(k) C(k), \quad (34)$$

where $C^\dagger = C^\dagger_\uparrow \oplus C^\dagger_\downarrow$ and $\hat{H}_{\text{BdG}} = \hat{H}_\uparrow \oplus \hat{H}_\downarrow$. The pseudospin-resolved Nambu operators are given by

$$C_s^\dagger(k) = (c_{k1,1s}^\dagger, c_{k1,2s}^\dagger, \dots, c_{kN,2s}^\dagger, \tilde{c}_{k1,1s}, \tilde{c}_{k1,2s}, \dots, \tilde{c}_{kN,2s}),$$

where $c_{ki,ns}^\dagger$ ($c_{ki,ns}$) creates (annihilates) an electron with momentum $k = k_x$ at position $i = i_y = 1, \dots, N_y$ in band $n = 1, 2$ with pseudospin $s = \uparrow, \downarrow$, and

$$\hat{H}_{\uparrow(\downarrow)} = \begin{pmatrix} \hat{\xi}_{\uparrow(\downarrow)} & \hat{\Delta}_{\uparrow(\downarrow)} \\ \hat{\Delta}_{\uparrow(\downarrow)}^\dagger & -\hat{\xi}_{\uparrow(\downarrow)} \end{pmatrix}. \quad (35)$$

The exact forms for the $2N_y \times 2N_y$ matrices $\hat{\xi}_{\uparrow(\downarrow)}$ and $\hat{\Delta}_{\uparrow(\downarrow)}$ are provided in Appendix D, for both the s - and d_{xy} -wave cases.

The BdG Hamiltonian \hat{H}_{BdG} is diagonal in the pseudospin space, with the blocks \hat{H}_\uparrow and \hat{H}_\downarrow being related by TR [see Eq. (17)]. Furthermore, it is diagonal in k space. As a consequence, the problem is reduced to the diagonalization of a $4N_y \times 4N_y$ matrix. Here, we employ an exact diagonalization procedure to solve for the eigenvalues as well as the corresponding eigenstates of $\hat{H}_\uparrow(k)$.

We begin the discussion of our results with the s -wave case. For a weak interband pairing, the spectrum is fully gapped in both the generic (see Sec. III A) and the exceptional cases (see Sec. III C). In the generic case, this situation remains true regardless of the strength of the interband pairing. In contrast, in the exceptional case, there exist two critical values, $\tilde{\eta}_{c,1}$ and $\tilde{\eta}_{c,2}$, between which the spectrum is gapless for four distinct k values (three k values at $\tilde{\eta} = \tilde{\eta}_{c,1}$ and two k values at $\tilde{\eta} = \tilde{\eta}_{c,2}$). As the interband pairing strength increases from $\tilde{\eta}_{c,1}$ to

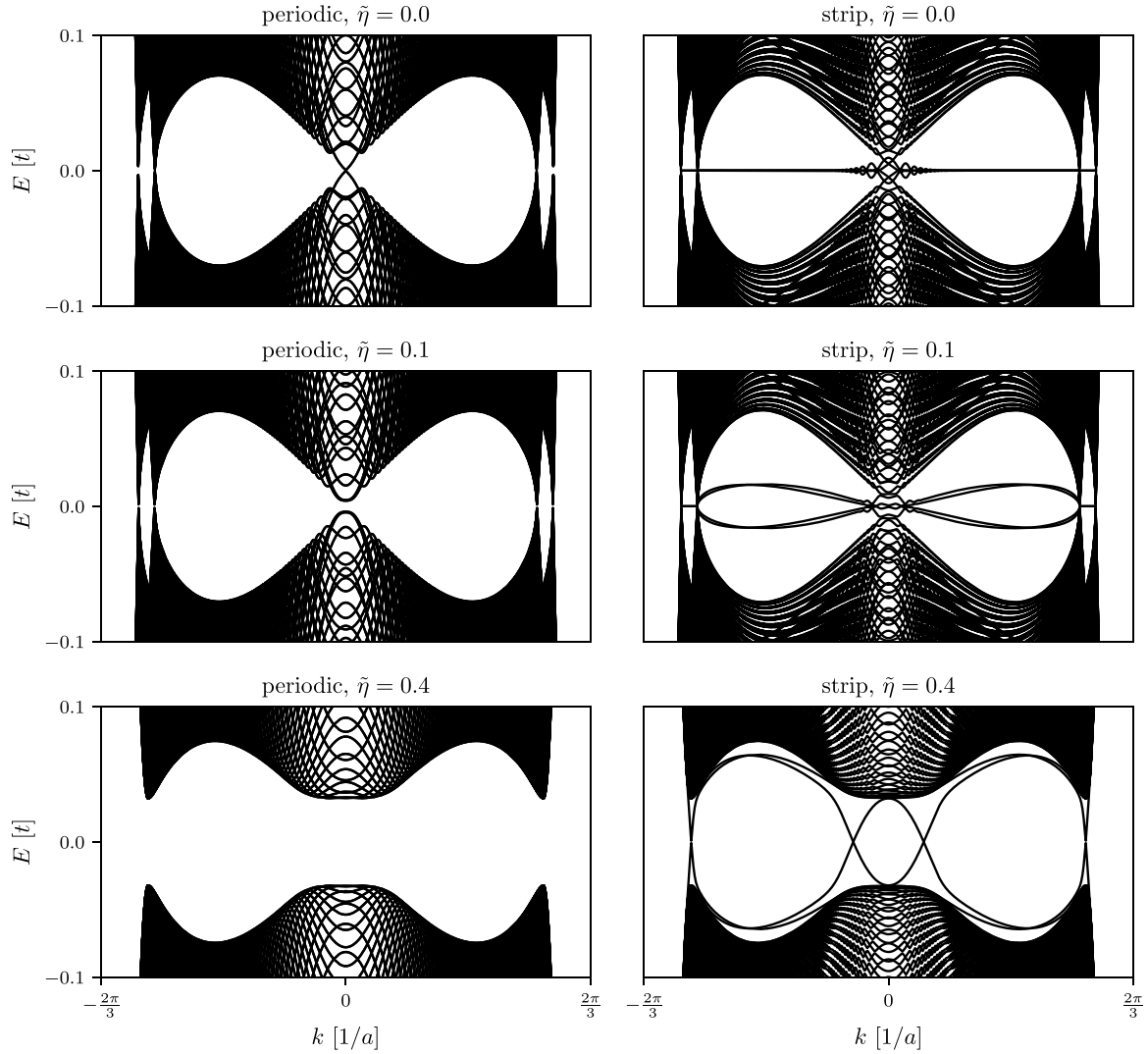


FIG. 4. Energy spectrum of $\hat{H}_\uparrow(k)$ [see Eq. (35)] in the generic d_{xy} -wave case, for increasing interband pairing $\tilde{\eta}$ (top to bottom). Left column: periodic boundary conditions. Right column: strip geometry. Parameters: $N_x = 2501$, $N_y = 500$, $\mu = -1.5$, $t_1 = 1.2$, $t_2 = 0.8$, $t'_1 = 0.5$, $t'_2 = 0.0$, $\eta_1 = 0.11$, $\eta_2 = -0.09$, $\rho = 0.5$. Energy is measured in the units of $t = (t_1 + t_2)/2$.

$\tilde{\eta}_{c,2}$, these nodes move towards each other until they annihilate eventually, so that the spectrum is fully gapped again. There are no edge states present—regardless of the interband pairing strength.

Next, we discuss the generic d_{xy} -wave case (see Sec. III B). The results are summarized in Fig. 4. In the absence of interband pairing (the top panels), the energy spectrum shows five zeros at $k_{LO} < k_{LI} < k_0 \equiv 0 < k_{RI} < k_{RO}$ (L, left; R, right; O, outer; I, inner). These correspond to the bulk nodes along the main axes and are located exactly on the two Fermi surfaces. The node at k_0 is fourfold degenerate corresponding to the four nodes of the system along the y direction. Between k_{LO} and k_{RO} the spectrum shows flat ABSs. As soon as the interband pairing is turned on, the ABSs between k_{LI} and k_{RI} gap out, while they remain intact between k_{LO} and k_{LI} as well as between k_{RI} and k_{RO} . Therefore, the zero-energy ABSs between the “inner” bulk nodes are topologically unstable (see Sec. V A).

As the interband pairing strength increases, the nodes move away from the Fermi surfaces until they meet each other and

annihilate. After this point, the bulk is completely gapped but eight zero-energy crossing ABS branches remain. They are singly degenerate (doubly degenerate for $\hat{H}_\uparrow \oplus \hat{H}_\downarrow$ if both edges are taken into account, as shown in Fig. 5) and the corresponding eigenstates are localized near the edges of the strip (see Appendix D). They mark a different, topologically nontrivial, superconducting phase.

The edge states in the gapped phase are schematically illustrated in Fig. 5. For \hat{H}_\uparrow , four states are located close to the left edge of the strip, while the other four are located close to the right edge of the strip. Depending on their slope they move either along the positive or negative x direction. Furthermore, they mix electrons from one band with holes from the other band (see Appendix D).

Finally, we turn our attention towards the exceptional d_{xy} -wave case (see Sec. III D). Similarly to the generic case, we observe a topological phase transition when the interband pairing strength increases. However, apart from the phase transition, the behavior of the spectrum significantly differs from the generic case. Weak interband pairing does not

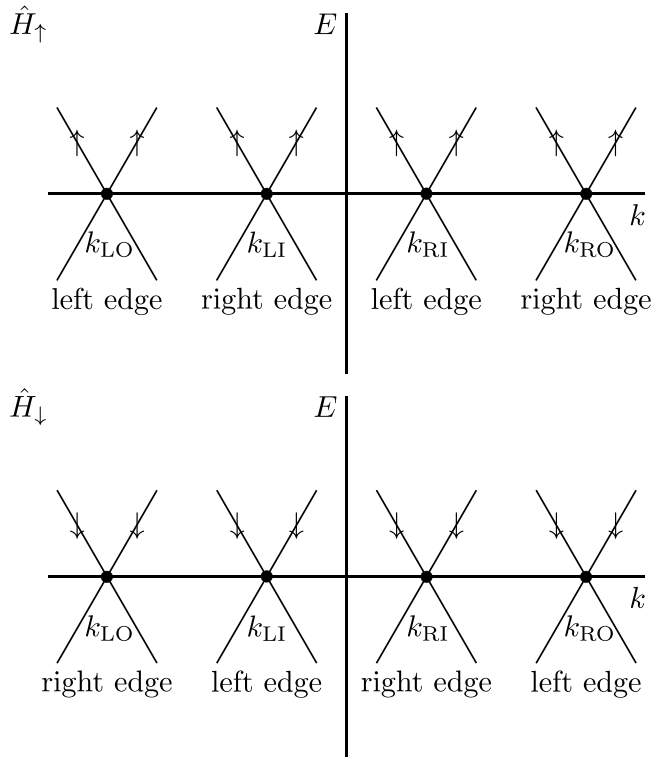


FIG. 5. Schematic illustration of the edge states in a fully gapped d_{xy} -wave SC, for strong interband pairing (top panel, the edge states for \hat{H}_\uparrow ; bottom panel, the edge states for \hat{H}_\downarrow).

immediately and fully gap out the ABSs. Indeed, there are ABSs present until the stray nodes annihilate along the diagonals of the Brillouin zone (see Sec. III D). As a comparison to the generic d_{xy} -wave case, we present the spectrum of the exceptional d_{xy} -wave case in Appendix D1.

We make two final remarks. First, the topological phase transition occurs regardless of the presence of TR symmetry. The characteristics of the edge states in the strip spectrum (see Fig. 4) are the same regardless of the intraband order parameter phases φ_n . Only the behavior of the bulk nodes and the ABSs in the gapless regime differs between the TR symmetry-breaking generic states and the TR-invariant exceptional states. Second, the interband pairing strength required to reach the topologically nontrivial superconducting phase strongly depends on the distance between the two Fermi surfaces. The closer the Fermi surfaces along the main axes of the Brillouin zone, the weaker the required interband pairing in order to annihilate the gap nodes.

V. TOPOLOGICAL ARGUMENTS

The results of the previous two sections show that the effects of the interband pairing are most profound in the d -wave states. The evolution of the bulk gap structure, which is reflected in the changes of the ABS spectrum, can be interpreted in terms of a series of transitions between topologically distinct superconducting phases. In this section, we discuss the relevant bulk topological invariants, focusing as before on the d_{xy} -wave states.

A. Gapless bulk

According to Sec. III, the bulk gap structure of a generic nodal d_{xy} -wave state is insensitive to the phases of the intraband order parameters: the nodes move on the high-symmetry axes as the interband pairing strength varies. In order to study the topological properties, one can focus on the TR invariant states, in which the order parameter components η_1 , η_2 , and $\tilde{\eta}$ are all real. If $\eta_1\eta_2 < 0$, then there exist only the high-symmetry nodes (Sec. III B), whereas at $\eta_1\eta_2 > 0$ the stray nodes are also possible (Sec. III D).

For the real order parameters, the Hamiltonians \hat{H}_\uparrow and \hat{H}_\downarrow [see Eq. (16)] have a ‘‘chiral’’ symmetry:

$$\hat{U}_S^\dagger \hat{H}_{\uparrow(\downarrow)} \hat{U}_S = -\hat{H}_{\uparrow(\downarrow)}(\mathbf{k}), \quad \hat{U}_S = \begin{pmatrix} \hat{\tau}_2 & 0 \\ 0 & \hat{\tau}_2 \end{pmatrix}.$$

In the basis in which \hat{U}_S is diagonal, the Hamiltonians can be brought to a block off-diagonal form, e.g.,

$$\hat{H}_\uparrow(\mathbf{k}) \rightarrow \hat{V} \hat{H}_\uparrow(\mathbf{k}) \hat{V}^\dagger = \begin{pmatrix} 0 & \hat{v}(\mathbf{k}) \\ \hat{v}^\dagger(\mathbf{k}) & 0 \end{pmatrix},$$

where

$$\hat{V} = \frac{1}{\sqrt{2}} \begin{pmatrix} 1 & -i & 0 & 0 \\ 0 & 0 & 1 & -i \\ -i & 1 & 0 & 0 \\ 0 & 0 & -i & 1 \end{pmatrix}$$

and

$$\hat{v} = \begin{pmatrix} \psi_1 + i\xi_1 & |\tilde{\Delta}|e^{i\tilde{\varphi}} \\ |\tilde{\Delta}|e^{-i\tilde{\varphi}} & \psi_2 + i\xi_2 \end{pmatrix}. \quad (36)$$

The v matrix for \hat{H}_\downarrow is obtained from Eq. (36) by replacing $\tilde{\varphi} \rightarrow -\tilde{\varphi}$.

The positions of the gap nodes are determined by the zeros of $|\det \hat{v}|$, whereas the topological charges of the nodes are given by the winding number of the phase of $\det \hat{v}$:

$$q = \oint \frac{d\mathbf{k}}{2\pi i} \nabla_{\mathbf{k}} \ln \det \hat{v} \quad (37)$$

(see Refs. [53,54]). The integration here is performed around an infinitesimally small circular contour wrapping counterclockwise around the node. From Eq. (36), we have

$$\det \hat{v} = \psi_1\psi_2 - \xi_1\xi_2 - |\tilde{\Delta}|^2 + i(\xi_1\psi_2 + \xi_2\psi_1), \quad (38)$$

where $\psi_n(\mathbf{k}) = \eta_n\alpha(\mathbf{k})$, assuming the same intraband symmetry factors in both bands. In agreement with the results of Sec. III, we see that the zeros of $|\det \hat{v}|$ are located in the interband space, either where $\alpha = 0$ and $\xi_1\xi_2 + \tilde{\Delta}^2 = 0$ (the high-symmetry nodes), or away from the symmetry axes (the stray nodes), the latter being possible only if η_1 and η_2 have the same sign.

The topological charges of the nodes can be easily calculated by expanding $\det \hat{v}(\mathbf{k})$ in the vicinity of the nodes. In the case $\eta_1 > 0$, $\eta_2 < 0$, we find (see Appendix E) that the gap nodes located on the same axis are oppositely ‘‘charged,’’ as shown in Figs. 6–8, which makes it possible for the nodes to annihilate each other, as discussed in Sec. III B.

According to Refs. [53,54], the number of the zero-energy edge modes at given momentum k_x along the boundary, per

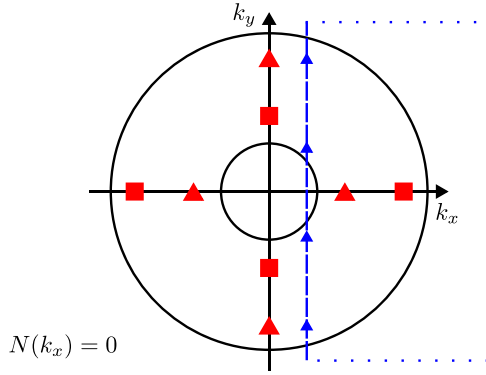


FIG. 6. Integration contour for computing the topological invariant $N(k_x)$ [see Eq. (40)]. Red triangles and squares: gap node positions at finite interband pairing $0 < \tilde{\eta} < \tilde{\eta}_c$ (generic d_{xy} -wave case). The different shapes indicate that the nodes have opposite topological charges.

one pseudospin projection, is equal to $|N(k_x)|$, where

$$N(k_x) = \text{Im} \int_{-\infty}^{\infty} \frac{dk_y}{2\pi} \nabla_{k_y} \ln \det \hat{v}(\mathbf{k}). \quad (39)$$

The integral here is taken along a straight line which runs between the opposite edges of the Brillouin zone perpendicular to the boundary. In a continuum model, the limits are extended to infinity. Assuming that all gap functions vanish far from the Fermi surfaces, one can integrate along a closed contour C shown in Figs. 6–8. Using the Stokes theorem to contract the contour without crossing any gap nodes, we find that $N(k_x)$ is equal to the total charge of the nodes enclosed by C .

In this way, we obtain

$$|N(k_x)| = \begin{cases} 0, & \text{at } |k_x| < k_2, \\ 1, & \text{at } k_2 < |k_x| < k_1, \\ 0, & \text{at } k_1 < |k_x|, \end{cases} \quad (40)$$

where $k_{1,2}$ are the positions of the bulk nodes [see Eq. (25)]. Taking into account the pseudospin degeneracy, the total number of the zero-energy ABS localized near one edge of the

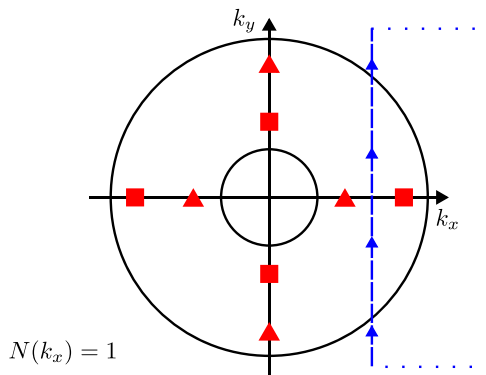


FIG. 7. Integration contour for computing the topological invariant $N(k_x)$ [see Eq. (40)]. Red triangles and squares: gap node positions at finite interband pairing $0 < \tilde{\eta} < \tilde{\eta}_c$ (generic d_{xy} -wave case). The different shapes indicate that the nodes have opposite topological charges.

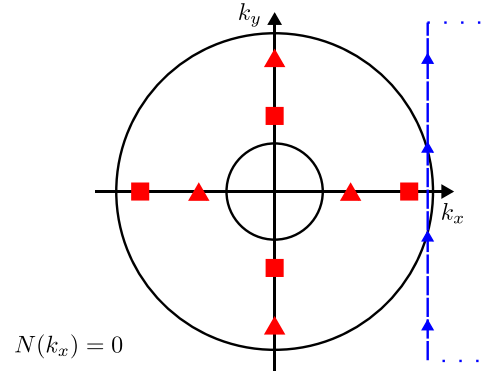


FIG. 8. Integration contour for computing the topological invariant $N(k_x)$ [see Eq. (40)]. Red triangles and squares: gap node positions at finite interband pairing $0 < \tilde{\eta} < \tilde{\eta}_c$ (generic d_{xy} -wave case). The different shapes indicate that the nodes have opposite topological charges.

sample is equal to $2|N(k_x)|$. We see that the momentum range in which the topologically protected zero-energy boundary modes exist shrinks with increasing the interband pairing and eventually disappears, in agreement with the numerical results of Sec. IV.

In the d -wave case with $\eta_1\eta_2 > 0$ (see Sec. III D), any two gap nodes located on the same high-symmetry axis have the same topological charges, until one of the nodes reverses the sign of its charge by shedding two stray nodes at some strength of the interband pairing, as explained in Appendix E. One can repeat the arguments leading to Eq. (40) and obtain that in the presence of the stray nodes, the zero-energy ABSs are topologically protected if k_x is between the innermost and outermost projections of the stray nodes onto the boundary.

In the nodal s -wave case considered in Sec. III C, one can show that the topological charges of the accidental nodes shown in Fig. 2 have alternating signs along the circle (28). Therefore, $N(k_x) = 0$ at all k_x and there are no zero-energy ABSs.

B. Gapped bulk

We have seen in the previous sections that the bulk Bogoliubov spectrum becomes fully gapped when the interband pairing exceeds a certain value. Moreover, if $\tilde{\Delta} \neq 0$, then the Bogoliubov branches E_+ and E_- [see Eq. (19)] are always separated. In the absence of any level crossings, the intraband pairing can be adiabatically turned off without affecting the bulk topology. Therefore, in order to study the topology of the mappings $\mathbf{k} \rightarrow \hat{H}_\uparrow(\mathbf{k})$ and $\mathbf{k} \rightarrow \hat{H}_\downarrow(\mathbf{k})$ in the nodeless regime, we can set $\eta_1 = \eta_2 = 0$, which considerably simplifies the calculations. The pseudospin-resolved Hamiltonians (16) are then reduced to direct sums of 2×2 matrices:

$$\hat{H}_\uparrow(\mathbf{k}) = \hat{h}_\uparrow^+(\mathbf{k}) \oplus \hat{h}_\uparrow^-(\mathbf{k}), \quad \hat{H}_\downarrow(\mathbf{k}) = \hat{h}_\downarrow^+(\mathbf{k}) \oplus \hat{h}_\downarrow^-(\mathbf{k}),$$

where

$$\begin{aligned} \hat{h}_\uparrow^\pm &= \pm \frac{\xi_1 - \xi_2}{2} \hat{\sigma}_0 + \mathbf{v}_\pm \hat{\boldsymbol{\sigma}}, \\ \hat{h}_\downarrow^\pm &= \mp \frac{\xi_1 - \xi_2}{2} \hat{\sigma}_0 + \mathbf{v}_\pm \hat{\boldsymbol{\sigma}}, \end{aligned} \quad (41)$$

and $\mathbf{v}_\pm = (\tilde{\eta}\tilde{\alpha}, \mp\tilde{\eta}\tilde{\beta}, \xi)$ and $\xi = (\xi_1 + \xi_2)/2$. Since the Hamiltonians \hat{H}_\uparrow and \hat{H}_\downarrow are in the class C, the gapped bulk states are characterized by an even ($2\mathbb{Z}$) topological invariant [49]. Therefore, we expect an even number of zero-energy boundary modes.

In the case of the d_{xy} -wave pairing, we have

$$\tilde{\alpha} \pm i\tilde{\beta} = \sin(2\theta) \pm i\rho \cos(2\theta) \quad (42)$$

[see Eqs. (11) and (8)]. Therefore, the matrices (41) have the same form as the BdG Hamiltonians for the chiral $d \pm id$ states, shifted up or down in energy. It is well known [55] that the $d + id$ and $d - id$ superconductors can support chiral boundary modes, which are protected by the bulk topology.

Diagonalizing Eq. (41) and using the band model (23), we find that the bulk spectra of \hat{H}_\uparrow and \hat{H}_\downarrow are the same and, in agreement with Eq. (19), are given by four particle-hole symmetric branches $\pm E_\pm$, where

$$E_\pm = \left| \sqrt{\xi^2 + |\tilde{\Delta}|^2} \pm \frac{\mathcal{E}_b}{2} \right|$$

and $\tilde{\Delta}$ has the form (18). Note that the branch indices in this last expression have nothing to do with the chirality index \pm in Eq. (41). At a sufficiently strong interband pairing, $|\tilde{\Delta}| > \mathcal{E}_b/2$, the bulk spectrum is fully gapped.

According to Refs. [35,56], the topological invariant characterizing a gapped chiral d -wave state has the following form:

$$N = \frac{1}{4\pi} \int d^2\mathbf{k} \hat{\mathbf{v}} \left(\frac{\partial \hat{\mathbf{v}}}{\partial k_x} \times \frac{\partial \hat{\mathbf{v}}}{\partial k_y} \right), \quad (43)$$

where $\hat{\mathbf{v}} = \mathbf{v}/|\mathbf{v}|$ and $\mathbf{v} = \mathbf{v}_+$ or \mathbf{v}_- . Here we integrate over the 2D momentum space, which can be compactified into an S^2 sphere, because the gap functions vanish outside the overlapping BCS pairing shells (see Sec. II), so that $\hat{\mathbf{v}} = \hat{\mathbf{z}} \text{sign } \xi$ and the integrand in Eq. (43) is equal to zero far from the Fermi surfaces. The expression (43) is nothing but the degree of the mapping $\mathbf{k} \rightarrow \hat{\mathbf{v}}(\mathbf{k})$, which takes integer values and can be used to enumerate different equivalence classes of the Hamiltonians (41).

Writing the interband gap functions in the form (18), with $|\tilde{\Delta}|$ nonvanishing only inside the pairing shells of thickness ϵ_c , Eq. (43) takes the form

$$N = \frac{1}{4\pi} \int d^2\mathbf{k} \frac{|\tilde{\Delta}|^2}{(\xi^2 + |\tilde{\Delta}|^2)^{3/2}} \left(\frac{\partial \xi}{\partial k_x} \frac{\partial \tilde{\varphi}}{\partial k_y} - \frac{\partial \xi}{\partial k_y} \frac{\partial \tilde{\varphi}}{\partial k_x} \right).$$

Finally, neglecting the ξ dependence of $|\tilde{\Delta}|$ and $\tilde{\varphi}$ inside the pairing shell, sending $\epsilon_c \rightarrow \infty$, and integrating with respect to ξ , we obtain

$$N = \frac{1}{2\pi} \oint d\tilde{\varphi}, \quad (44)$$

where the integration is performed along the $\xi = 0$ line. Since we neglect the ξ dependence of $\tilde{\varphi}$, one could integrate along either of the two Fermi surfaces, with the same result (note that the lines $\xi = 0$, $\xi_1 = 0$, and $\xi_2 = 0$ all lie within the BCS pairing shell, which encompasses both Fermi surfaces). Thus, the invariant (43) is equal to the phase winding number of the interband gap function.

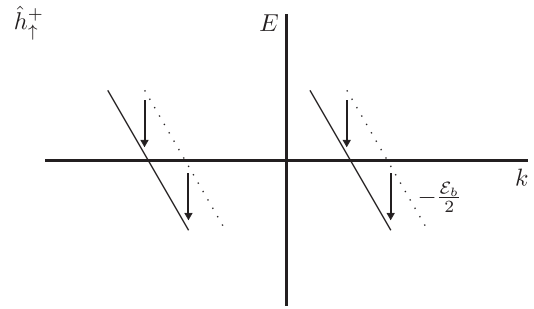


FIG. 9. Schematic illustration of the chiral edge modes for the Hamiltonian \hat{h}_\uparrow^+ [see Eq. (41)]. Dashed lines: chiral modes without the energy shift. Solid lines: chiral modes shifted by $-\mathcal{E}_b/2$.

For the d_{xy} -wave pairing [see Eq. (42)], we obtain the following winding numbers for \hat{h}_\uparrow^\pm and \hat{h}_\downarrow^\pm :

$$N_\pm = \mp 2 \text{sign } \rho.$$

Therefore, each of the four Hamiltonians \hat{h}_\uparrow^\pm and \hat{h}_\downarrow^\pm has two chiral zero modes near each edge of the sample. These modes have opposite slopes for opposite chiralities, and are also shifted up and down in energy by $\pm \mathcal{E}_b/2$, as shown in Fig. 9 for \hat{h}_\uparrow^+ and $\rho > 0$. The 4×4 Hamiltonian \hat{H}_s corresponding to one pseudospin channel has four helical modes composed of two pairs of the counterpropagating chiral modes from \hat{h}_s^+ and \hat{h}_s^- , as shown in Fig. 5. This result is in agreement with the numerical solution of the BdG equations (see Fig. 4).

VI. CONCLUSION

Based on a symmetry analysis, we determined the possible interband pairing gap functions in the case of two-band superconductors with s -wave, d_{xy} -wave, or $d_{x^2-y^2}$ -wave pairing, which can give rise to both TR invariant and TR symmetry-breaking superconducting states. As the interband pairing strength increases, the nodal structure changes fundamentally. Nodes leave the Fermi surfaces and eventually annihilate each other on the high-symmetry axes, whereas other nodes (stray nodes) appear, move, and merge in the interband space.

In the case of a d -wave superconductor with a strip geometry, the boundary modes exhibit qualitative changes when interband pairing increases. Starting from zero-energy flat ABSs in the absence of interband pairing, these modes partially gap out as soon as interband pairing is turned on. In the limit of strong interband pairing, the system undergoes a topological phase transition to a fully gapped helical $d \pm id$ -wave superconducting state. The corresponding topological invariant is the phase winding number of the interband gap, which explains the existence of the eight gap-crossing zero-energy branches near one edge of the sample in the helical state.

ACKNOWLEDGMENTS

We thank M. Fischer and A. Ramires for helpful discussions. This work was supported by the Swiss National Science Foundation through Division II (Grant No. 184739) (M.H. and M.S.) and by Discovery Grant No. 2021-03705 from the Natural Sciences and Engineering Research Council of

Canada (K.S.). K.S. is grateful to the Institute for Theoretical Physics, ETH Zurich for hospitality and the Pauli Center for Theoretical Studies for financial support.

APPENDIX A: RESPONSE TO TR

Suppose that the triplet component of the interband gap function is given by $\boldsymbol{\beta} = (0, 0, \tilde{\beta})$ (see Secs. II A and II B). Then, the pairing Hamiltonian (3) takes the following form:

$$\begin{aligned} \hat{H}_{\text{SC}} = & \frac{1}{2} \sum_k [\eta_1 \alpha_1 (c_{k,1\uparrow}^\dagger \tilde{c}_{k,1\uparrow}^\dagger + c_{k,1\downarrow}^\dagger \tilde{c}_{k,1\downarrow}^\dagger) \\ & + \eta_2 \alpha_2 (c_{k,2\uparrow}^\dagger \tilde{c}_{k,2\uparrow}^\dagger + c_{k,2\downarrow}^\dagger \tilde{c}_{k,2\downarrow}^\dagger) \\ & + \tilde{\eta}(\tilde{\alpha} + i\tilde{\beta})(c_{k,1\uparrow}^\dagger \tilde{c}_{k,2\uparrow}^\dagger + c_{k,2\downarrow}^\dagger \tilde{c}_{k,1\downarrow}^\dagger) \\ & + \tilde{\eta}(\tilde{\alpha} - i\tilde{\beta})(c_{k,1\downarrow}^\dagger \tilde{c}_{k,2\downarrow}^\dagger + c_{k,2\uparrow}^\dagger \tilde{c}_{k,1\uparrow}^\dagger)] + \text{H.c.} \end{aligned}$$

Since $K(c_{k,ns}^\dagger \tilde{c}_{k,n's'}^\dagger)K^{-1} = c_{k,n's'}^\dagger \tilde{c}_{k,ns}^\dagger$, the TR-transformed Hamiltonian is given by

$$\begin{aligned} K\hat{H}_{\text{SC}}K^{-1} = & \frac{1}{2} \sum_k [\eta_1^* \alpha_1 (c_{k,1\uparrow}^\dagger \tilde{c}_{k,1\uparrow}^\dagger + c_{k,1\downarrow}^\dagger \tilde{c}_{k,1\downarrow}^\dagger) \\ & + \eta_2^* \alpha_2 (c_{k,2\uparrow}^\dagger \tilde{c}_{k,2\uparrow}^\dagger + c_{k,2\downarrow}^\dagger \tilde{c}_{k,2\downarrow}^\dagger) \\ & + \tilde{\eta}(\tilde{\alpha} - i\tilde{\beta})(c_{k,2\uparrow}^\dagger \tilde{c}_{k,1\uparrow}^\dagger + c_{k,1\downarrow}^\dagger \tilde{c}_{k,2\downarrow}^\dagger) \\ & + \tilde{\eta}(\tilde{\alpha} + i\tilde{\beta})(c_{k,2\downarrow}^\dagger \tilde{c}_{k,1\downarrow}^\dagger + c_{k,1\uparrow}^\dagger \tilde{c}_{k,2\uparrow}^\dagger)] + \text{H.c.} \end{aligned}$$

which is the same as \hat{H}_{SC} , with $(\eta_1, \eta_2, \tilde{\eta})$ replaced by $(\eta_1^*, \eta_2^*, \tilde{\eta}^*)$. If the order parameter is real, then $K\hat{H}_{\text{SC}}K^{-1} = \hat{H}_{\text{SC}}$, i.e., the Hamiltonian is intrinsically complex, but TR invariant.

APPENDIX B: STABLE STATES

The three order parameter components can be combined into $\boldsymbol{\eta} = (\eta_1, \eta_2, \tilde{\eta})^\top$. The second- and fourth-order uniform terms in the GL free energy density have the following form:

$$F_2 = \boldsymbol{\eta}^\dagger \hat{A} \boldsymbol{\eta}, \quad \hat{A} = \begin{pmatrix} A_{11} & A_{12} & \tilde{A}_{13} \\ A_{12} & A_{22} & \tilde{A}_{23} \\ \tilde{A}_{13} & \tilde{A}_{23} & \tilde{A}_{33} \end{pmatrix}, \quad (\text{B1})$$

where \hat{A} is a real symmetric matrix and

$$\begin{aligned} F_4 = & \beta_1 |\eta_1|^4 + \beta_2 |\eta_2|^4 + \tilde{\beta}_1 |\eta_1|^2 |\tilde{\eta}|^2 + \tilde{\beta}_2 |\eta_2|^2 |\tilde{\eta}|^2 \\ & + \tilde{\beta}_3 |\tilde{\eta}|^4 + \tilde{\beta}_4 (\eta_1 \eta_2 \tilde{\eta}^{*2} + \text{c.c.}) \end{aligned}$$

(see Ref. [32] for the microscopic derivation). The diagonal elements of the matrix \hat{A} depend on temperature, so that \hat{A} loses positive definiteness at the critical temperature T_c . In the absence of the interband pairing, all the quantities with tildes are zero and Eq. (B1) takes the usual form for a two-band superconductor, with A_{12} describing the Josephson tunneling of the Cooper pairs between the bands.

Choosing $\tilde{\eta}$ to be real positive, neglecting the quartic terms, and writing the intraband order parameters in the form (21),

the phase-dependent terms in the energy can be represented as

$$F(\varphi_1, \varphi_2) = a \cos(\varphi_1 - \varphi_2) + \tilde{a}_1 \cos \varphi_1 + \tilde{a}_2 \cos \varphi_2, \quad (\text{B2})$$

where a , \tilde{a}_1 , and \tilde{a}_2 are proportional to the off-diagonal elements of \hat{A} and can be positive or negative. Minimizing Eq. (B2), we obtain

$$\begin{aligned} a \sin(\varphi_1 - \varphi_2) + \tilde{a}_1 \sin \varphi_1 &= 0, \\ a \sin(\varphi_1 - \varphi_2) - \tilde{a}_2 \sin \varphi_2 &= 0. \end{aligned} \quad (\text{B3})$$

These equations always have four solutions $\varphi_1, \varphi_2 = 0$ or π , which correspond to the TR invariant superconducting states. Whether these states are stable or not depends on the parameters in Eq. (B2).

In general, Eq. (B3) can also have solutions different from 0 or π , which describe TR symmetry-breaking superconducting states. To construct these solutions, we employ the following procedure. First, we pick some values of φ_1 and φ_2 and use Eq. (B3) to obtain

$$\tilde{a}_1 = -a \frac{\sin(\varphi_1 - \varphi_2)}{\sin \varphi_1}, \quad \tilde{a}_2 = a \frac{\sin(\varphi_1 - \varphi_2)}{\sin \varphi_2}. \quad (\text{B4})$$

If the coefficients satisfy these relations, then the energy (B2) has a critical point at the given (φ_1, φ_2) . Next, we check if this critical point is a minimum by calculating the second derivatives of the function (B2). Using Eq. (B4), we obtain that the Hessian matrix is positive definite if

$$\text{sign}(a) \frac{\sin \varphi_1}{\sin \varphi_2} < 0. \quad (\text{B5})$$

Taking any point (φ_1, φ_2) from the stability regions defined by this last inequality and substituting it in Eq. (B4), we find the GL energy for which this pair of phases delivers a minimum (local or global).

One can easily show that the solutions satisfying Eq. (B5) exist only if $a\tilde{a}_1\tilde{a}_2 > 0$, i.e., if

$$\text{sign}(A_{12}\tilde{A}_{13}\tilde{A}_{23}) > 0.$$

In other words, we have proved that if the number of negative quadratic intercomponent couplings in Eq. (B1) is even, then our system can have TR symmetry-breaking superconducting states, which are at least locally stable.

Also, we note that the TR symmetry-breaking states with $\varphi_1 + \varphi_2 = 0$ discussed in Sec. III can only exist at the special values of the coefficients, namely, if $\tilde{a}_1 = \tilde{a}_2$. Therefore, such states are unstable against a small variation of the system's parameters, e.g., the temperature.

APPENDIX C: BULK ENERGY SPECTRUM

Assuming a real $\tilde{\eta}$, the BdG Hamiltonian (16) in either pseudospin channel can be represented in the form

$$\hat{H} = \begin{pmatrix} \mathbf{v}_1 \hat{\sigma} & \tilde{\Delta} \hat{\sigma}_1 \\ \tilde{\Delta}^* \hat{\sigma}_1 & \mathbf{v}_2 \hat{\sigma} \end{pmatrix}, \quad (\text{C1})$$

where $\mathbf{v}_n = (\text{Re}\psi_n, -\text{Im}\psi_n, \xi_n)$. It is manifestly particle-hole symmetric and one can find its spectrum either by a direct calculation of a 4×4 determinant [43] or by using the following trick [57].

Let us calculate the second and fourth powers of Eq. (C1):

$$\hat{H}^2 = \begin{pmatrix} \mu_1 \hat{\sigma}_0 & \hat{m} \\ \hat{m}^\dagger & \mu_2 \hat{\sigma}_0 \end{pmatrix},$$

where $\mu_n = v_n^2 + |\tilde{\Delta}|^2$, $\hat{m} = \tilde{\Delta}(\mathbf{v}_1 \hat{\sigma}_1 + \mathbf{v}_2 \hat{\sigma}_1 \hat{\sigma})$, and

$$\hat{H}^4 = \begin{pmatrix} \mu_1^2 \hat{\sigma}_0 + \hat{m} \hat{m}^\dagger & (\mu_1 + \mu_2) \hat{m} \\ (\mu_1 + \mu_2) \hat{m}^\dagger & \mu_2^2 \hat{\sigma}_0 + \hat{m}^\dagger \hat{m} \end{pmatrix}.$$

One can see that the matrix $\hat{M} = \hat{H}^4 - (\mu_1 + \mu_2) \hat{H}^2$ does not contain off-diagonal 2×2 blocks. Moreover, since

$$\hat{m} \hat{m}^\dagger = \hat{m}^\dagger \hat{m} = |\tilde{\Delta}|^2 [(\mathbf{v}_1 - \mathbf{v}_2)^2 + 4v_{1,1}v_{2,1}] \hat{\sigma}_0,$$

we find that \hat{M} is proportional to the 4×4 unit matrix. Therefore, the eigenvalues of \hat{H} satisfy the following bi-quadratic equation:

$$E^4 - (\mu_1 + \mu_2)E^2 + \mu_1\mu_2 - |\tilde{\Delta}|^2 [(\mathbf{v}_1 - \mathbf{v}_2)^2 + 4v_{1,1}v_{2,1}] = 0.$$

Solving it, we obtain the Bogoliubov energy branches given by Eq. (19).

APPENDIX D: BDG FORMALISM IN THE STRIP GEOMETRY

The $2N_y \times 2N_y$ matrices $\hat{\xi}_{\uparrow(\downarrow)}$ and $\hat{\Delta}_{\uparrow(\downarrow)}$ appearing in the BdG Hamiltonian (34) are of the form

$$\hat{\xi}_{\uparrow(\downarrow)} = \begin{pmatrix} \hat{\xi}_{+0\uparrow(\downarrow)} & \hat{\xi}_{+1\uparrow(\downarrow)} & & \\ \hat{\xi}_{-1\uparrow(\downarrow)} & \ddots & \ddots & \\ & \ddots & \ddots & \ddots \end{pmatrix},$$

which is block tridiagonal, and

$$\hat{\Delta}_{\uparrow(\downarrow)} = \begin{pmatrix} \hat{\Delta}_{+0\uparrow(\downarrow)} & \hat{\Delta}_{+1\uparrow(\downarrow)} & \hat{\Delta}_{+2\uparrow(\downarrow)} & & \\ \hat{\Delta}_{-1\uparrow(\downarrow)} & \ddots & \ddots & \ddots & \\ \hat{\Delta}_{-2\uparrow(\downarrow)} & \ddots & \ddots & \ddots & \ddots \\ & \ddots & \ddots & \ddots & \ddots \end{pmatrix},$$

which is block quinquidiagonal. The labels $+0, \pm 1, \pm 2$ refer to the respective (off)diagonals of the matrices $\hat{\xi}_{\uparrow(\downarrow)}$ and $\hat{\Delta}_{\uparrow(\downarrow)}$. Furthermore, regardless of the superconducting pairing we have

$$\begin{aligned} \hat{\xi}_{+0\uparrow(\downarrow)} &= \left[-\frac{\mu_1 + \mu_2}{2} - (t_1 + t_2) \cos(k) \right] \hat{\tau}_0 \\ &+ \left[-\frac{\mu_1 - \mu_2}{2} - (t_1 - t_2) \cos(k) \right] \hat{\tau}_3, \\ \hat{\xi}_{+1\uparrow(\downarrow)} &= \left[-\frac{t_1 + t_2}{2} - (t'_1 + t'_2) \cos(k) \right] \hat{\tau}_0 \\ &+ \left[-\frac{t_1 - t_2}{2} - (t'_1 - t'_2) \cos(k) \right] \hat{\tau}_3, \end{aligned}$$

and $\hat{\xi}_{-1\uparrow(\downarrow)} = \hat{\xi}_{+1\uparrow(\downarrow)}^\dagger$, where $\hat{\tau}_i$ matrices refer to the band space.

Fermionic antisymmetry requires

$$\hat{\Delta}_{\uparrow(\downarrow)}(\mathbf{k}) = \hat{\Delta}_{\downarrow(\uparrow)}^\dagger(-\mathbf{k}),$$

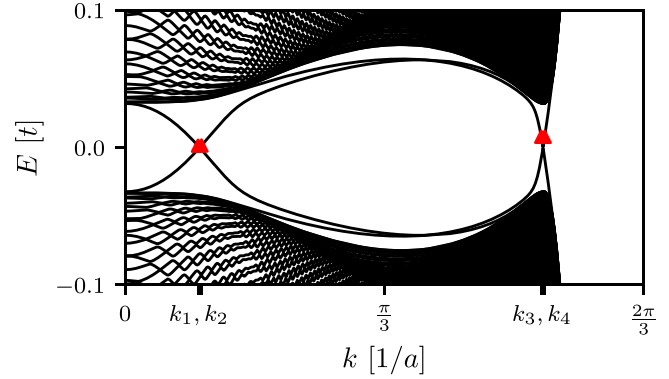


FIG. 10. Energy spectrum of $\hat{H}_\uparrow(k)$ [see Eq. (35)] in the generic d_{xy} -wave case, for the strip geometry at the interband pairing $\tilde{\eta} = 0.4$ (see bottom-right plot of Fig. 4). Red triangles: positions $k_1 < k_2 < k_3 < k_4$ for which the corresponding eigenstate profiles are shown in Fig. 11.

so that $\hat{\Delta}_{-1(-2)\uparrow(\downarrow)}(k) = \hat{\Delta}_{+1(+2)\downarrow(\uparrow)}^\dagger(-k)$. Therefore, in the s-wave case, we have

$$\hat{\Delta}_{+0\uparrow(\downarrow)}(k) = \frac{\eta_1 + \eta_2}{2} \hat{\tau}_0 + \tilde{\eta} \hat{\tau}_1 + \frac{\eta_1 - \eta_2}{2} \hat{\tau}_3,$$

$$\hat{\Delta}_{+1\uparrow(\downarrow)}(k) = \pm \frac{i}{2} \rho \tilde{\eta} \sin(k) \cos(k) \hat{\tau}_2,$$

$$\hat{\Delta}_{+2\uparrow(\downarrow)}(k) = \mp \frac{i}{4} \rho \tilde{\eta} \sin(k) \hat{\tau}_2,$$

while in the d_{xy} -wave case, we have

$$\hat{\Delta}_{+0\uparrow(\downarrow)}(k) = \mp \rho \tilde{\eta} \cos(k) \hat{\tau}_2,$$

$$\begin{aligned} \hat{\Delta}_{+1\uparrow(\downarrow)}(k) &= \pm \frac{1}{2} \rho \tilde{\eta} \hat{\tau}_2 - \frac{i}{2} \sin(k) \\ &\times \left[\frac{\eta_1 + \eta_2}{2} \hat{\tau}_0 + \tilde{\eta} \hat{\tau}_1 + \frac{\eta_1 - \eta_2}{2} \hat{\tau}_3 \right], \end{aligned}$$

$$\hat{\Delta}_{+2\uparrow(\downarrow)}(k) = 0.$$

If periodic boundary conditions are also considered along the y direction (i.e., the strip is closed to a torus), then additional off-diagonal terms appear in the corners of $\hat{\xi}_{\uparrow(\downarrow)}$ and $\hat{\Delta}_{\uparrow(\downarrow)}$.

Figure 10 illustrates that the gap-crossing energy branches in the strong interband-pairing regime belong to states which are localized near the edges of the strip. The respective eigenstates ψ of the Hamiltonian \hat{H}_\uparrow are of size $4N_y$ and split into electron and hole contributions as well as band contributions $n = 1$ and 2 , as shown in Fig. 11.

1. Spectrum of the exceptional d_{xy} -wave case

We have included the spectrum of the exceptional d_{xy} -wave case in Fig. 12 for completeness. To compare it with the spectrum of the generic d_{xy} -wave case in Fig. 4, we have used the same parameters for the numerical simulation except that the relative phase between the two intraband order parameters is now zero.

In the absence of interband pairing (as shown in the top panels), the energy spectrum displays five zeros, similar to the generic d_{xy} -wave case. These correspond to the bulk nodes

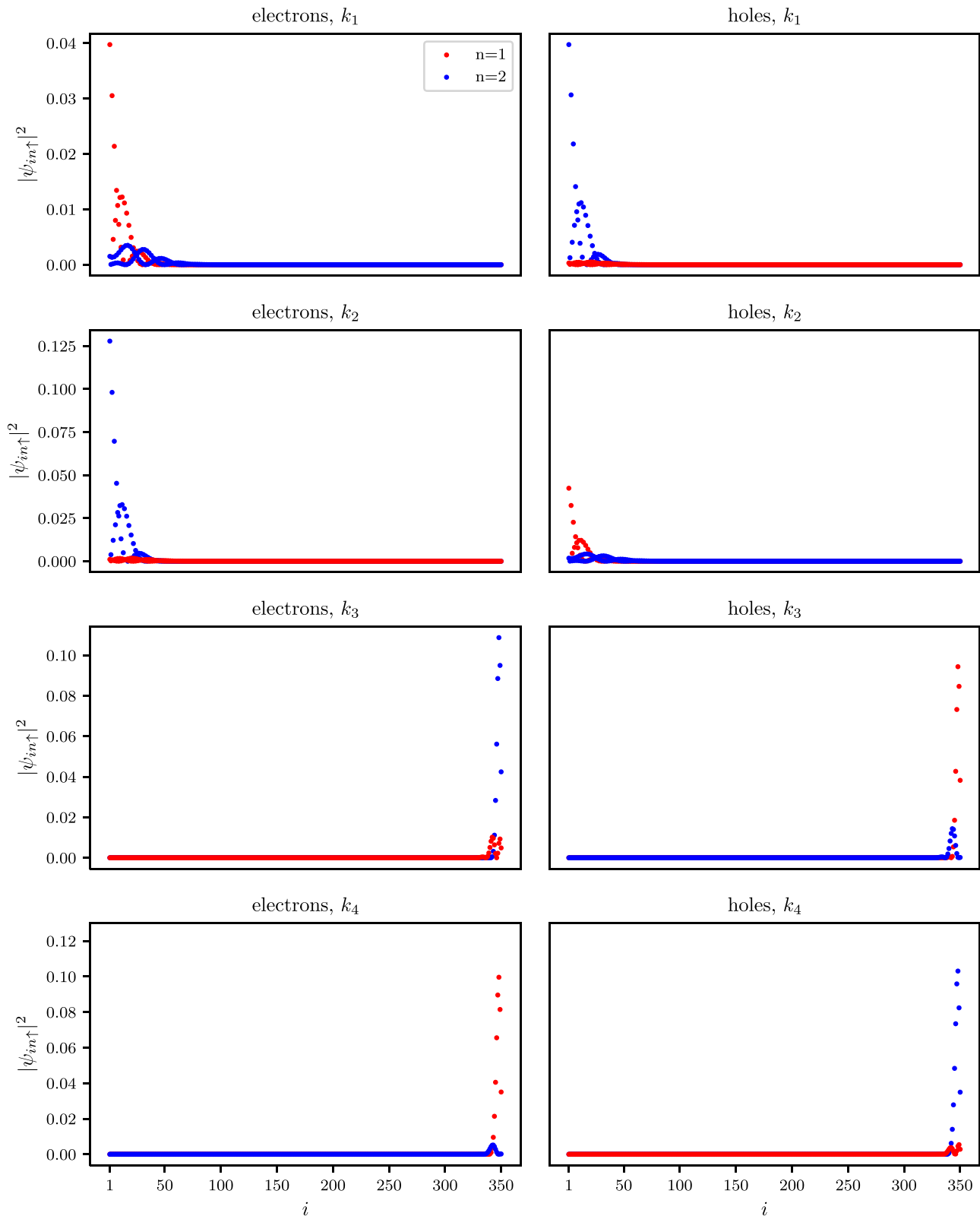


FIG. 11. Eigenstate profiles of the states marked by red dots in Fig. 10 as a function of y position. Left column: electron components of the eigenstates. Right column: hole components of the eigenstates.

along the main axes and are located exactly on the two Fermi surfaces. The node at $k = 0$ is fourfold degenerate corresponding to the four nodes of the system along the y direction.

However, when interband pairing is turned on, the inner zero-energy ABSs do not completely gap out, unlike the generic d_{xy} -wave case. The reason is that the nodes located on the

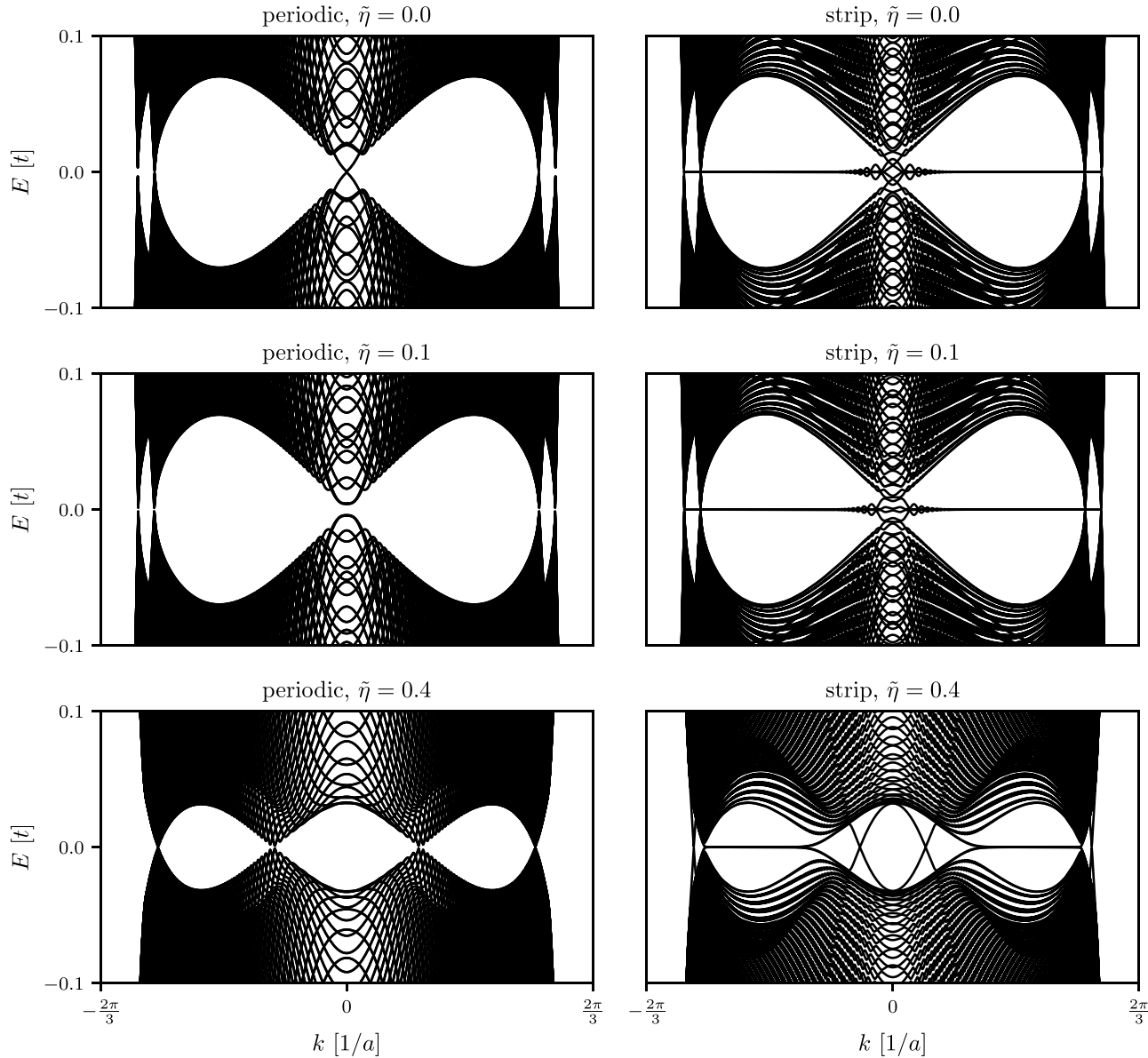


FIG. 12. Energy spectrum of $\hat{H}_\gamma(k)$ [see Eq. (35)] in the exceptional d_{xy} -wave case, for increasing interband pairing $\tilde{\eta}$ (top to bottom). Left column: periodic boundary conditions. Right column: strip geometry. Parameters: $N_x = 2501$, $N_y = 500$, $\mu = -1.5$, $t_1 = 1.2$, $t_2 = 0.8$, $t'_1 = 0.5$, $t'_2 = 0.0$, $\eta_1 = 0.11$, $\eta_2 = 0.09$, $\rho = 0.5$. Energy is measured in the units of $t = (t_1 + t_2)/2$.

same high-symmetry axis have the same topological charge (see Appendix E). The inner ABSs persist until the stray nodes annihilate each other off the high-symmetry axes, as discussed in Sec. III D.

The bottom panels of Fig. 12 correspond to the situation when the interband pairing is sufficiently strong, so that the high-symmetry nodes have all annihilated each other and only the stray nodes remain in the interband space. The flat zero-energy ABSs shown in the bottom-right panel connect the projections of those stray nodes onto the k_x axis. Eventually, for even stronger interband pairing (not shown in Fig. 12), the bulk spectrum gaps out and we observe the same topological phase transition as in the generic d -wave case, with only the helical ABS branches remaining.

APPENDIX E: TOPOLOGICAL CHARGES OF THE NODES

Substituting Eqs. (23) and (24) in Eq. (38), we obtain

$$\begin{aligned} \det \hat{v} = & \left(\frac{\mathcal{E}_b}{2}\right)^2 - \tilde{\eta}^2[\rho^2 + (1 - \rho^2)\sin^2(2\theta)] \\ & - \xi^2 + \eta_1\eta_2\sin^2(2\theta) \\ & + i\left[\left(\xi + \frac{\mathcal{E}_b}{2}\right)\eta_1 + \left(\xi - \frac{\mathcal{E}_b}{2}\right)\eta_2\right]\sin(2\theta), \end{aligned} \quad (\text{E1})$$

with real η_1 and η_2 . Equating the real and imaginary parts of this last expression to zero, we recover the results of Sec. III B, if $\eta_1\eta_2 < 0$, and Sec. III D, if $\eta_1\eta_2 > 0$.

Let us consider, for example, the high-symmetry nodes along the positive k_x axis, i.e., at $\theta = 0$. They are located between the two Fermi surfaces, at $\xi = \pm\xi_0$, where

$$\xi_0 = \sqrt{\left(\frac{\mathcal{E}_b}{2}\right)^2 - \tilde{\eta}^2 \rho^2}.$$

We expand Eq. (E1) near the nodes by setting $\xi = \pm\xi_0 + \xi_0 x$, $\theta = y$ ($|x|, |y| \ll 1$), and obtain $\det \hat{v} = \mp \xi_0^2 (x + iw_{\pm} y)$, where

$$w_{\pm} = -\frac{1}{\xi_0^2} \left[\left(\xi_0 \pm \frac{\mathcal{E}_b}{2} \right) \eta_1 + \left(\xi_0 \mp \frac{\mathcal{E}_b}{2} \right) \eta_2 \right]. \quad (\text{E2})$$

Therefore, the topological charges of the nodes [see Eq. (37)] are given by

$$q_{\pm} = \text{sign}(w_{\pm}).$$

In particular, in the absence of the interband pairing, we have $q_+ = -\text{sign}(\eta_1)$ and $q_- = -\text{sign}(\eta_2)$.

It follows from Eq. (E2) that

$$q_+ q_- = \text{sign} \left[\eta_1 \eta_2 - \frac{\tilde{\eta}^2 \rho^2}{\mathcal{E}_b^2} (\eta_1 + \eta_2)^2 \right]. \quad (\text{E3})$$

If η_1 and η_2 have opposite signs, then $q_+ q_- < 0$, independently of the value of $\tilde{\eta}$. The high-symmetry nodes on the same axis have opposite charges and annihilate each other at the critical strength of the interband pairing, given by Eq. (26).

In contrast, if η_1 and η_2 have the same sign, then Eq. (E3) changes sign at

$$\tilde{\eta}_c = \frac{\mathcal{E}_b}{|\rho|} \frac{\sqrt{|\eta_1 \eta_2|}}{|\eta_1| + |\eta_2|}.$$

At this value of the interband pairing, one of the high-symmetry nodes splits into two stray nodes of the same charge and one high-symmetry node of the opposite charge (see Sec. III D). All nodes eventually annihilate one another at a sufficiently strong interband pairing.

-
- [1] J. Nagamatsu, N. Nakagawa, T. Muranaka, Y. Zenitani, and J. Akimitsu, Superconductivity at 39 K in magnesium diboride, *Nature (London)* **410**, 63 (2001).
- [2] S. L. Bud'ko and P. C. Canfield, Superconductivity of magnesium diboride, *Physica C* **514**, 142 (2015).
- [3] P. C. Canfield, P. L. Gammel, and D. J. Bishop, New magnetic superconductors: A toy box for solid-state physicists, *Phys. Today* **51**(10), 40 (1998).
- [4] A. P. Mackenzie and Y. Maeno, The superconductivity of Sr_2RuO_4 and the physics of spin-triplet pairing, *Rev. Mod. Phys.* **75**, 657 (2003).
- [5] D. F. Agterberg, T. M. Rice, and M. Sigrist, Orbital dependent superconductivity in Sr_2RuO_4 , *Phys. Rev. Lett.* **78**, 3374 (1997).
- [6] C. Kallin and A. J. Berlinsky, Is Sr_2RuO_4 a chiral p -wave superconductor? *J. Phys.: Condens. Matter* **21**, 164210 (2009).
- [7] E. Boaknin, M. A. Tanatar, J. Paglione, D. Hawthorn, F. Ronning, R. W. Hill, M. Sutherland, L. Taillefer, J. Sonier, S. M. Hayden, and J. W. Brill, Heat conduction in the vortex state of NbSe_2 : Evidence for multiband superconductivity, *Phys. Rev. Lett.* **90**, 117003 (2003).
- [8] W. Shi, J. Ye, Y. Zhang, R. Suzuki, M. Yoshida, J. Miyazaki, N. Inoue, Y. Saito, and Y. Iwasa, Superconductivity series in transition metal dichalcogenides by ionic gating, *Sci. Rep.* **5**, 12534 (2015).
- [9] M. A. Tanatar, J. Paglione, S. Nakatsuji, D. G. Hawthorn, E. Boaknin, R. W. Hill, F. Ronning, M. Sutherland, L. Taillefer, C. Petrovic, P. C. Canfield, and Z. Fisk, Unpaired electrons in the heavy-fermion superconductor CoCoIn_5 , *Phys. Rev. Lett.* **95**, 067002 (2005).
- [10] E. Bauer, G. Hilscher, H. Michor, C. Paul, E. W. Scheidt, A. Griбанov, Y. Seropegin, H. Noël, M. Sigrist, and P. Rogl, Heavy fermion superconductivity and magnetic order in non-centrosymmetric CePt_3Si , *Phys. Rev. Lett.* **92**, 027003 (2004).
- [11] M. R. Norman, High-temperature superconductivity in the iron pnictides, *Physics* **1**, 21 (2008).
- [12] P. J. Hirschfeld, M. M. Korshunov, and I. I. Mazin, Gap symmetry and structure of Fe-based superconductors, *Rep. Prog. Phys.* **74**, 124508 (2011).
- [13] L. A. Wray, S.-Y. Xu, Y. Xia, D. Hsieh, A. V. Fedorov, Y. S. Hor, R. J. Cava, A. Bansil, H. Lin, and M. Z. Hasan, A topological insulator surface under strong coulomb, magnetic and disorder perturbations, *Nat. Phys.* **7**, 32 (2011).
- [14] L. Fu and E. Berg, Odd-parity topological superconductors: Theory and application to $\text{Cu}_x\text{Bi}_2\text{Se}_3$, *Phys. Rev. Lett.* **105**, 097001 (2010).
- [15] H. Suhl, B. T. Matthias, and L. R. Walker, Bardeen-Cooper-Schrieffer theory of superconductivity in the case of overlapping bands, *Phys. Rev. Lett.* **3**, 552 (1959).
- [16] V. A. Moskalenko, Superconductivity for overlapping electron bands, *Fiz. Met. Metalloved.* **8**, 503 (1959) [*Phys. Met. Metallogr.* **8**, 25 (1959)].
- [17] A. J. Leggett, Number-phase fluctuations in two-band superconductors, *Prog. Theor. Phys.* **36**, 901 (1966).
- [18] Y. Tanaka, Soliton in two-band superconductor, *Phys. Rev. Lett.* **88**, 017002 (2001).
- [19] E. Babaev, Vortices with fractional flux in two-gap superconductors and in extended Faddeev model, *Phys. Rev. Lett.* **89**, 067001 (2002).
- [20] Y. Tanaka, Multicomponent superconductivity based on multiband superconductors, *Supercond. Sci. Technol.* **28**, 034002 (2015).
- [21] O. V. Dolgov, E. P. Fetsiov, D. I. Khomskii, and K. Svozil, Model of interband pairing in mixed valence and heavy fermion systems, *Z. Phys. B* **67**, 63 (1987).
- [22] A. Moreo, M. Daghofer, A. Nicholson, and E. Dagotto, Interband pairing in multiorbital systems, *Phys. Rev. B* **80**, 104507 (2009).
- [23] M. H. Fischer, Gap symmetry and stability analysis in the multiorbital Fe-based superconductors, *New J. Phys.* **15**, 073006 (2013).

- [24] T. Ong, P. Coleman, and J. Schmalian, Concealed d -wave pairs in the s^\pm condensate of iron-based superconductors, *Proc. Natl. Acad. Sci. USA* **113**, 5486 (2016).
- [25] A. Ramires and M. Sgrist, Identifying detrimental effects for multiorbital superconductivity: Application to Sr_2RuO_4 , *Phys. Rev. B* **94**, 104501 (2016).
- [26] T. Nomoto, K. Hattori, and H. Ikeda, Classification of “multipole” superconductivity in multiorbital systems and its implications, *Phys. Rev. B* **94**, 174513 (2016).
- [27] E. M. Nica, R. Yu, and Q. Si, Orbital-selective pairing and superconductivity in iron selenides, *npj Quantum Mater.* **2**, 24 (2017).
- [28] G.-Y. Zhu, F.-C. Zhang, and G.-M. Zhang, Proximity-induced superconductivity in monolayer CuO_2 on cuprate substrates, *Phys. Rev. B* **94**, 174501 (2016).
- [29] V. Stanev and Z. Tešanović, Three-band superconductivity and the order parameter that breaks time-reversal symmetry, *Phys. Rev. B* **81**, 134522 (2010).
- [30] S. Maiti and A. V. Chubukov, $s + is$ state with broken time-reversal symmetry in Fe-based superconductors, *Phys. Rev. B* **87**, 144511 (2013).
- [31] Y. Yerlin, A. Omelyanchouk, S.-L. Drechsler, D. V. Efremov, and J. van den Brink, Anomalous diamagnetic response in multiband superconductors with broken time-reversal symmetry, *Phys. Rev. B* **96**, 144513 (2017).
- [32] K. V. Samokhin, Ginzburg-Landau energy of multiband superconductors with interband pairing, *Phys. Rev. B* **109**, 134508 (2024).
- [33] M. Sgrist and K. Ueda, Phenomenological theory of unconventional superconductivity, *Rev. Mod. Phys.* **63**, 239 (1991).
- [34] V. Mineev and K. V. Samokhin, *Introduction to Unconventional Superconductivity* (Gordon and Breach, New York, 1999).
- [35] G. E. Volovik, *The Universe in a Helium Droplet* (Oxford University, New York, 2009).
- [36] B. A. Bernevig, *Topological Insulators and Topological Superconductors* (Princeton University, Princeton, NJ, 2013).
- [37] S. Kashiwaya and Y. Tanaka, Tunnelling effects on surface bound states in unconventional superconductors, *Rep. Prog. Phys.* **63**, 1641 (2000).
- [38] J. A. Sauls, Andreev bound states and their signatures, *Phil. Trans. R. Soc. A* **376**, 20180140 (2018).
- [39] C. Kittel, *Quantum Theory of Solids* (Wiley, New York, 1987).
- [40] M. Lax, *Symmetry Principles in Solid State and Molecular Physics* (Dover, New York, 2001).
- [41] K. Ueda and T. M. Rice, p -wave superconductivity in cubic metals, *Phys. Rev. B* **31**, 7114 (1985).
- [42] K. V. Samokhin, Symmetry of superconducting pairing in non-pseudospin electron bands, *Phys. Rev. B* **100**, 054501 (2019).
- [43] K. V. Samokhin, Exotic interband pairing in multiband superconductors, *Phys. Rev. B* **101**, 214524 (2020).
- [44] A. A. Vargas-Paredes, A. A. Shanenko, A. Vagov, M. V. Milosević, and A. Perali, Crossband versus intraband pairing in superconductors: Signatures and consequences of the interplay, *Phys. Rev. B* **101**, 094516 (2020).
- [45] P. Fulde and R. A. Ferrell, Superconductivity in a strong spin-exchange field, *Phys. Rev.* **135**, A550 (1964).
- [46] A. I. Larkin and Y. N. Ovchinnikov, Inhomogeneous state of superconductors, *Zh. Eksp. Teor. Fiz.* **47**, 1136 (1964) [*Sov. Phys.-JETP* **20**, 762 (1965)].
- [47] A. Altland and M. R. Zirnbauer, Nonstandard symmetry classes in mesoscopic normal-superconducting hybrid structures, *Phys. Rev. B* **55**, 1142 (1997).
- [48] A. Kitaev, Periodic table for topological insulators and superconductors, *AIP Conf. Proc.* **1134**, 22 (2009).
- [49] S. Ryu, A. P. Schnyder, A. Furusaki, and A. W. W. Ludwig, Topological insulators and superconductors: Tenfold way and dimensional hierarchy, *New J. Phys.* **12**, 065010 (2010).
- [50] A. V. Chubukov, O. Vafek, and R. M. Fernandes, Displacement and annihilation of Dirac gap nodes in d -wave iron-based superconductors, *Phys. Rev. B* **94**, 174518 (2016).
- [51] T. Nakayama, T. Shishidou, and D. F. Agterberg, Nodal topology in d -wave superconducting monolayer FeSe, *Phys. Rev. B* **98**, 214503 (2018).
- [52] M. F. Holst, M. Sgrist, and M. H. Fischer, Role of topology and symmetry for the edge currents of a two-dimensional superconductor, *Phys. Rev. Res.* **4**, 013244 (2022).
- [53] M. Sato, Y. Tanaka, K. Yada, and T. Yokoyama, Topology of Andreev bound states with flat dispersion, *Phys. Rev. B* **83**, 224511 (2011).
- [54] A. P. Schnyder and S. Ryu, Topological phases and surface flat bands in superconductors without inversion symmetry, *Phys. Rev. B* **84**, 060504(R) (2011).
- [55] G. E. Volovik, On edge states in superconductors with time inversion symmetry breaking, *JETP Lett.* **66**, 522 (1997).
- [56] M. Sgrist, Aspects of topological superconductivity, in *Lecture Notes of the Autumn School on Correlated Electrons Topology, Entanglement, and Strong Correlations* (Julich, Germany, 2020).
- [57] C. F. B. Lo, H. C. Po, and A. H. Nevidomskyy, Inherited topological superconductivity in two-dimensional Dirac semimetals, *Phys. Rev. B* **105**, 104501 (2022).